The dynamics of energetic electron precipitation during substorms MONOGRAPH

Utilization of the remote sensing technique of X rays

N. Østgaard

Abstract. Based on the remote sensing technique of X rays this thesis is devoted to the study of the dynamics of energetic precipitation during substorms. In this monograph the remote sensing techniques at different wavelengths are discussed, with emphasize on their ability to infer spectral information about the electron precipitation. Previous studies about the energetic precipitation are reviewed in order to put the 5 papers that constitutes the thesis in a scientific historical context. It is found that the development of substorms does not reveal the same characteristics when examining different electron energies. This is obvious from a case study of the substorm triggering process based on multi-satellite measurements. Onsets and intensifications of precipitation during substorms may not always involve both soft and energetic electrons and hence onsets can be identified differently when examining different energies. The difference in solar wind input energy prior to the events seems to be important for the differences observed. From a statistical study when comparing ultraviolet emission and X rays a localized maximum of energetic electron precipitation in the morning sector delayed with respect to substorm onset is clearly seen in the X-ray aurora, but only occasionally in the ultraviolet substorm. The time delay of this morning precipitation relative to substorm onset strongly indicates that this intensification is related to electrons injected in the midnight sector drifting into the dawnside magnetosphere. To explain the morning maximum of X-ray emission it is suggested that the unstably quasi-trapped electrons cause growth of VLF waves, which act back on the electrons and effectively scatter them into the loss cone. In contrast to the other remote sensing techniques at other wavelengths the derivation of electron energy information from X rays provide a multi-parameter representation of the electron precipitation, and thus determines both the low- and high-energy range of the electron spectrum. Contrary to the auroral emissions at other wavelengths that are contaminated by sunlight or sunlight generated emissions, the auroral X rays can successfully be detected both at the dayside and the nightside of the Earth. Thus X rays are found to be favourable in estimating the global energy input into the ionosphere.

1. Introduction

This thesis is devoted to the study of energetic electron precipitation during substorms utilizing the remote sensing technique of X rays. A main goal of this thesis has been to evaluate the properness of the X-ray measurements and to develop tools to extract spectral information about the energetic electron precipitation that has generated the X rays. With the use of these tools spatial and temporal information about the X-ray features can provide new insight about the dynamics of the energetic electron precipitation. While other remote sensing techniques like ultraviolet and visible imaging sense emissions that are dominantly produced by low energy electrons (<10 keV), the X-ray imagers respond to electrons of higher energies. The two X-ray experiments described in this thesis measured X rays in the energy range from 5.6 keV up to 100 keV (Pulsaur II, rocket experiment [Stadsnes et al., 1995]) and from ~3 keV up to ~60 keV (The Polar Ionospheric X-ray Imaging Experiment, PIXIE [Imhof et al., 1995]). As this is X-ray bremsstrahlung produced by the precipitating energetic electrons into the ionosphere the two instruments respond to electrons above 5.6 keV and 3 keV, respectively. From the measured X rays it is possible to derive a multi-parameter electron spectrum directly from the X-ray spectrum, as the production of X rays is quite well understood theoretically. Even though the probability of generating an X-ray photon from an electron slowing down in the atmosphere increases as a function of the initial electron energy, a 200 keV electron only deposits 0.5% of its energy as X rays [Berger and Seltzer, 1972]. Thus the X-ray measurements very often suffer from poor statistics. Nevertheless these measurements provide the opportunity to study the energetic electron precipitation, even in the sunlit area. The Pulsaur II experiment was a rocket experiment flown during the recovery phase of a substorm at ~0130 MLT to study the pulsating aurora during a 9 min flight. Based on the simultaneous measurements of X rays and electrons with relatively good spatial and temporal resolution, this experiment enabled us to study the correspondence between the electron precipitation and the generation of X rays in detail. The PIXIE instrument is flown on the Polar satellite, and due to its highly elliptical orbit (1.8 x 9 R_E) the PIXIE camera provides global images of the X-ray aurora for about 12 hours during an apogee pass and for about 40 minutes during a perigee pass. As PIXIE is a true two-dimensional X-ray imager, this instrument provides the first possibility ever to study the global dynamics of energetic electron precipitation during substorms and storms. Hence, another main goal of this thesis has been to utilize this possibility to obtain new insight about the global characteristics of the energetic precipitation.

The thesis consists of 3 published papers and 2 submitted papers, which present the scientific results from the two experiments (1 from Pulsaur II and 4 from PIXIE, plus a technical report on the image processing method developed for the PIXIE measurements). In Section 2 we describe the different global remote sensing techniques used in the space science over the last two decades and discuss their benefits and disadvantages. In Section 3 we review some earlier studies describing the behaviour of energetic electron precipitation in order to put our results in a scientific historical context. In Section 4 the main results from the Pulsaur II experiment are discussed, while Section 5 is devoted to PIXIE, the image processing and the scientific results obtained from this experiment so far. In Section 6 we conclude and suggest some future studies based on the PIXIE data.

2. Global remote sensing techniques in substorm studies

When using the term global remote sensing techniques we do not include the different kind of remote sensing provided by ground-based equipment like magnetometers, riometers detecting cosmic radio noise absorption or radar, because they do not provide any global information unless a lot of stations are used simultaneously. We restrict ourselves to the remote sensing techniques used in space by imaging instruments flown on spacecrafts in order to study the global features of substorm dynamics, i.e., satellites orbiting the Earth at a few hundred km of altitude up to many Earth radii. From the first global imaging instrument was flown in

1973 on board the ISIS-2 satellite [Anger et al., 1973] a lot of missions equipped with instruments measuring at different wavelengths have been flown in space. Summaries of some important parameters of the visible, UV and X-ray imagers flown in space are listed in Tables 1 and 2. The tables show the development of imagers towards better temporal and spatial resolution as well as that the area covered by the imagers has increased. All emissions detected by these imaging instruments are caused by the particle precipitation into the ionosphere along field lines which can be traced into the equatorial plane of the magnetosphere. Thus, from the dynamics of the features of emission at different wavelengths in the ionosphere it is possible to extract information about the magnetospheric processes that determines acceleration, convection, scattering and precipitation of these particles in the magnetosphere. As the various emissions respond to particles in different energy ranges these imaging techniques provide information on how the various particle energies behave differently in the magnetosphere. Detecting specific wavelengths of auroral emissions involves certain techniques and methods for interpreting the measurements, which all have their benefits and disadvantages. In this section we will describe and discuss the properties of some of the auroral emissions in the visible, the UV and the X-ray wavelengths, and their benefits and disadvantages in order to extract information about the parent electron distribution.

Table 1. Summary of various auroral (visible and UV) imagers (From Frank et al. [1995], Torr et al. [1995] and the Internet)

Imager/ Satellite	Angular resolution degrees	Spacecraft altitude	Wavelength Å	Image frame rate	Noise equivalent signal[a]	Reference
ISIS-2	0.4	1400 km	3914, 5577, 6300	100 min	300 R	Anger et al. 1973
DMSP	0.25	850 km	4000-11 300	100 min	-	Rogers et al. 1974
KYOKKO (EXOS-A)	0.3	650-4000 km	1200-1400	128 s	-	Kaneda et al. 1977
DE	0.29	1-4 R_E	1216-6300 several filters	12 min	1 KR	Frank et al., 1981
HILAT	1.7	830 km	1100 -1900 scanning	100 min	25-60 R	Meng and Huffman, 1984
Polar BEAR	-	1000 km	-	-	-	Meng et al., 1987
Viking	0.08	15 000 km	1235-1600 1340-1800	20 s	-	Anger et al., 1987
Acebono (EXOS-D)	0.1	300-10 000 km	1150-1600 5577	8-16 s	300 R at 1216 50 R at 5577	Oguti et al., 1990
FREJA	0.08	600-1700 km	1340-1800 2 filters:	6 s	700 R	-
Interball-2 UVAI	-	~0.2-3.2 R_E	1250-1600	60 s	-	Optical design: Anger et al., 1987
UVI	0.03	1-8 R_E	1300-1900 4 filters	37 s	10 R	Torr et al., 1995
VIS	0.01-0.02	1-8 R_E	3914, 5577, 6300 6563, 7320	12 s	130 R - 1 kR	Frank et al., 1995

[a] Threshold at which the signal is equal to the instrument noise in an integration period

Table 2. Summary of various X-ray imagers flown on satellites (Based on Imhof et al. [1995], Stadsnes et al. [1997] and the Internet)

Imager/ Satellite	Ionospheric area detected	Spacial resolution at 100 km altitude	Spacecraft altitude	Energy range keV	Time resolution	Reference
1972-076B	Collimated detector on a spinning satellite (one look direction)	-	~750 km	> 50	100 min	Imhof et al., 1974
DMSP F-2	Only nadir	-	830 km	1.4-90	100 min	Mizera et al., 1978
P 78-1	Array of 8 detectors, to each side of the spinning satellite	130-330 km	600 km	>21	100 min	Imhof et al., 1980
SEEP/XRIS S81-1	One dimensional pinhole camera, oriented cross track 500 km wide area.	30 km	170-270 km	4-40	100 min	Calvert et al., 1985
DMSP F-6, GFE-6	cross track scanning	-	830 km	-	100 min	Mizera et al., 1984
UARS PEM/AXIS	Array of 16 detectors, oriented cross track	<100 km	585 km	3-100	100 min	Chenette et al., 1992
PIXIE	Two dimensional pinhole camera, global images	1000 km (apogee) 150 km (perigee)	1-8 R_E	2-60	<5 min (apogee) <2min (perigee)	Imhof et al., 1995

2.1. Visible emissions

The visible aurora was originally studied from ground just as a broad band emission covering the entire visible spectrum. By the developing of filters and photo-multiplicators one was able to study the narrow band emissions which correspond to specific excitation levels of atomic and molecular states. The interpretation of the luminosity of these emission lines is then depending on our knowledge about the processes that leads to the excitation and the subsequently de-excitation and photon emission. Quenching and absorption must be understood and properly taken into account. Both the energy of the incoming electron, the height profile of different species in the atmosphere, chemical interactions at different altitudes are crucial for the interpretation of the measurements at different wavelengths. In Table 3 we have listed some of the emission lines in the visible spectrum which have been widely used for the auroral science, both from ground and in space.

Table 3. Four of the most common visible emission lines used to detect auroral patterns and dynamics (From Omholt [1971]).

Wavelength (Å)	Species	Excitation energy (eV)	Lifetime (s)
3914	N_2^+	19	prompt
4278	N_2^+	19	prompt
5577	O and O_2	4 and 9	0.7
6300	O	1.96	110

As can be seen from this table the excitation energies for the most common visible emission lines are all below some tens of eV, which means that these emissions are produced by both primary and secondary electrons. Thus the auroral emission at these lines is basically an integral response to the precipitation of electrons at all energies above the excitation energy, and not very strongly dependent on the electron energy spectrum. This is true for the prompt emissions, but not for emissions from the so-called metastable states, involving a time constant (e.g., the 5577 and 6300 emissions in Table 3) and the possibility of non-radiative quenching of the excitation when the excitation occurs deep in the atmosphere [Stadsnes et al., 1997]. Eather and Mende [1971] showed that the ratio of 4278/6300 emissions could be used to estimate the mean energy of the precipitating electrons. While the prompt N_2^+ emission line at 4278 Å is produced by all electron energies and therefore is proportional to the total energy flux, the O emission line at 6300 Å is strongly quenched through collisions below 200 km due to the long lifetime and only the electrons that are interacting above 200 km produces the 6300 emission line. Thus the luminosity of the 6300 emission line will be determined by the soft part of the electron energy spectrum and for a given total incident energy flux the luminosity depends strongly on the mean energy of the precipitating electrons. With the knowledge of height profile of O, relevant cross sections, loss processes for secondaries Rees and Luckey [1974] modelled the ratio of 4278/6300 emissions for Maxwellian electron distributions with mean energies in the energy range from 0.6 keV to 20 keV. Comparing measured ratios of 4278/6300 with the modelled ratios, the mean energy can be estimated. Models and measurements of the ratios 4278/5577, 3914/5577 and 3914/6300 emissions can also be used to estimate the mean energy of the incoming electrons. As an example Figure 1 shows the modelled ratio of 5577/4278 emissions deduced by Steele and McEwen [1990] and Rees and Luckey [1974] as presented by Robinson and Vondrak [1994] (their Figure 11). In a multi spectral study based on the visible imager (VIS) [Frank et al., 1995], the ultraviolet imager (UVI) [Torr et al., 1995] and PIXIE on board Polar, Cummer et al. [1999] have used the 3914 emission line to extract the total energy flux and the ratio of 3914/6300 emissions to derive the mean energy. They found the total precipitating electron energy flux and mean energy electron energy calculated from VIS, UVI and PIXIE to be in good (within 20%) agreement in most regions. As the spectrum of the incoming electrons falls rapidly off with increasing energies, the contribution to the luminosity from electrons >10 keV is very small and the effects on the ratios becomes even smaller. The visible emissions provide only two parameters to describe the electron precipitation, namely the total energy flux and the mean energy and the latter will mainly be determined by the shape of the spectrum <10 keV. Any information about the electron spectrum >10 keV can hardly be extracted from imaging the aurora at the visible wavelengths.

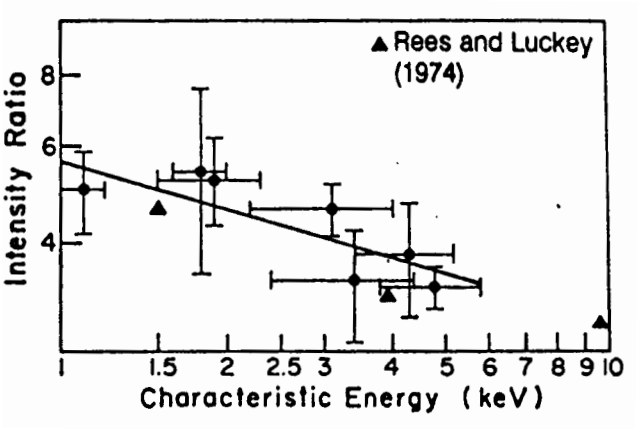

Figure 1. The ratio of 5577 Å to 4278 Å emissions as a function of Maxwellian characteristic energy deduced by Steele and McEwen [1990] (circles) compared with results of Rees and Luckey [1974] (triangles).

Due to the large albedo of sunlight at these wavelengths the visible imaging can only be provided during night time or wintertime when the hemisphere is dark all day. Atmospheric background may also cause some problem.

2.2. Ultraviolet emissions

The ultraviolet range of wavelengths contains two distinct oxygen emission lines (1304 Å and 1356 Å) and a lot of emission lines created dominantly by the electron impact on N_2, which are known as the Lyman-Birge-Hopfield (LBH) band. Figure 2 is a plot of the filter band pass for the UVI onboard the Polar satellite, showing both the two oxygen emission lines and the LBH band. Due to the improved filtering techniques used for the UVI instrument, the LBH band was separated into two broad UV emission bands, LBH-long (LBHL: 1600-1800 Å) and LBH-short (LBHS: 1400-1600 Å). As the O line at 1304 undergoes multiple scattering it has limited use for auroral imaging, but does have a potential as an indicator of the O concentration. The Lyman-Birge-Hopfield and the O 1356 emission line also undergo multiple scattering but the efficiency is relatively small [Strickland and Anderson, 1983]

and thus these wavelengths can be used for auroral imaging. As the Lyman-Birge-Hopfield band is dominated by the emissions created by the electron impact on N_2, all electron energies contribute in this process of prompt emissions. The luminosity of the LBH band is therefore proportional to the total electron energy flux. But as can be seen from Figure 2 the two bands, LBHL and LBHS and the O 1356 emission will be differently affected by the absorption by atmospheric oxygen. For the LBHL emission this absorption is very small and the intensity reflects approximately the total energy influx of electron precipitation [Germany et al., 1990; Germany et al., 1997]. As the lower electron energies usually dominate, the LBHL emissions provides the global features of the softer part of the electron distribution. On the other hand the LBHS band and O 1356 emission are strongly affected by the absorption by atmospheric oxygen. The attenuation of the radiation in the LBHS band and the O 1356 emissions increases as the incoming electrons deposit their energy deeper down in the atmosphere, i.e., with increasing electron energies. Thus the ratio of LBHL/LBHS (or LBHL/O 1356) can be used to extract spectral information about the electron precipitation. Modelling of expected emissions can be used to estimate the energy flux from LBHL intensity and the average energy from the ratio of either O 1356/LBHL or LBHS/LBHL [Germany et al., 1990]. In Figure 3 the ratio of LBHL/LBHS is shown as a function of average electron energies (E_{AV}) from 1-9 keV as modelled by G. Germany (private communication, 1999). Gaussian electron spectra of 1 erg cm^{-2} peaked at E_{AV} with a full width half maximum (FWHM) of 0.5 $[ln2]^{1/2}$ E_{AV} has been used to model the incident electron precipitation. As the electron energy flux usually falls off >10 keV the ratio of LBHL/LBHS (and LBHL/O 1356) becomes uncertain in the energy range >10 keV.

In the ideal case, the energy analysis would be performed with two LBH bands, one at the wavelength of peak absorption and the other at a longer wavelength where O_2 absorption is negligible. The longer wavelength emission would be essentially independent of average energy and solely dependent on energy flux. In practice, the LBH filters must necessarily include multiple emissions in the LBH band and therefore contain a range of loss factors. Thus the LBHL emissions show a weak dependence with average energy and though this effect is small (<10% at 10 keV) it must be taken into account to extract the energy parameters properly. For images from UVI on board Polar a look-up table, where this effect is included, has been used to provide maps of energy parameters [Germany et al., 1997].

The lower threshold energy for detecting LBH emissions (both long and short) is determined by the altitude profile of the N_2 versus O density. At high altitudes the density of O exceeds the density of N_2 and the competition between the O and the N_2 emissions determines the intensity of LBH emissions. Given an energy flux of 1 ergs cm^{-2} the threshold for UVI is about 1 keV and for larger energy fluxes the threshold may be lowered down to ~100 eV (G. Germany private communication, 1998). The upper threshold energy is determined by the decreasing electron flux >10 keV and the absorption by O_2 at low altitudes.

Even though the albedo of UV emissions (<1700 Å) is negligible, there is a significant contamination from sunlight generated UV emissions (dayglow). Thus the UV imaging is most successfully provided during night time [G. Germany private communication, 1999].

2.3. X rays

Precipitating electrons deposit their energy into the atmosphere

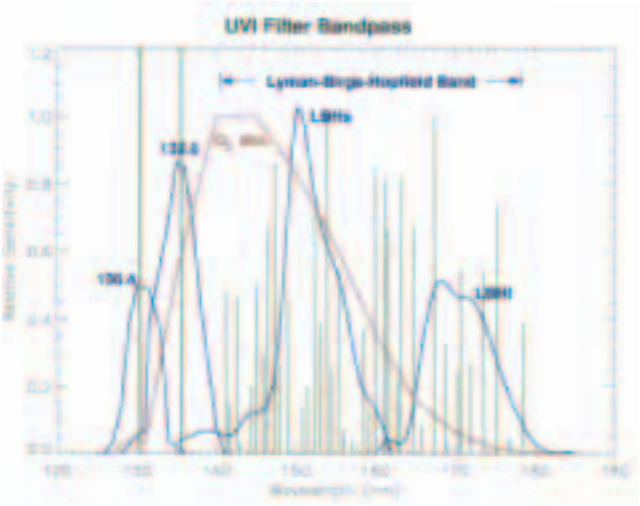

Figure 2. The filter bandpass for the UVI on board the Polar satellite. The four narrow band UVI filters are shown in blue and the red line shows the absorption by O_2. Green vertical show the discrete emission lines (M. Brittnacher private communication, 1998).

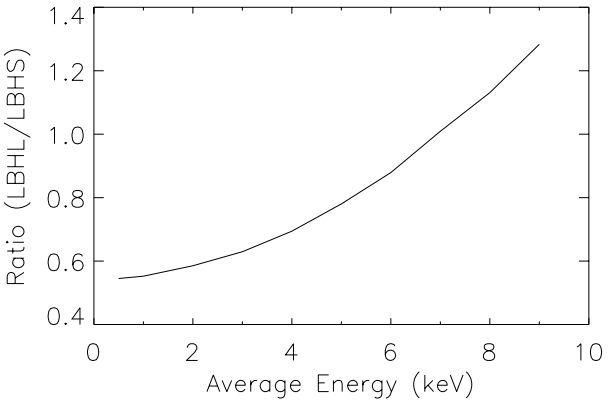

Figure 3. The ratio of LBHL/LBHS as a function of the average energy of the incoming electrons [G. Germany private communication, 1999].

by ionization, excitation, heating of the neutral gas and X-ray bremsstrahlung. X rays are produced by high energy primary electrons, while the other energy depositions involve both primary and secondary electrons over a wide energy range. The number of X-ray photons (n) that are generated by an electron with an initial energy (E_E) slowing down in the atmosphere, is rather small. For example, $n(E_E$=200 keV) = 0.0052 and $n(E_E$=20 keV) = 0.000057 [Berger and Seltzer, 1972]. Nevertheless, X-ray measurements are very useful in the study of the electron precipitation and information about the spectra, as well as spatial and temporal structures in the electron precipitation, can be obtained. Another advantage is that X rays can be detected in daylight. For these reasons the X-ray measurements are favourable in the study of energetic electron precipitation. A major problem with the global scale X-ray imaging, e.g., the PIXIE camera, is the statistics. In order to obtain sufficient counts either the spatial or the temporal resolution have to suffer. However, by using properly defined integration area the

time resolution can be as good as ~30 s, which is comparable to the time resolution of the two other imaging techniques. Regarding spatial resolution in order to study fine structures, the visible and UV imagers are still superior to the X-ray imagers, due to the much higher fluxes of these emissions.

As balloon and rocket experiments have recorded auroral X rays since about 1960, there has been a need for models that calculate the X-ray production from electron precipitation. Several models using different approximations and simplifications have been developed in order to calculate the yield of X rays from electron spectra [Rees, 1964; Kamiyama, 1966; Berger et al., 1970; Berger and Seltzer, 1972; Seltzer and Berger, 1974; Luhmann and Blake, 1977; Walt et al., 1979; Khosa et al., 1984; Robinson et al., 1989; Gorney, 1987; Lorence, 1992]. Experiments have been performed to make simultaneous measurements of electrons and X rays [e.g. Vij et al., 1975; Mizera et al., 1978; Goldberg et al., 1982; Datlowe et al., 1988], and the comparisons between measured and calculated X rays have resulted in different degree of agreement. Generally the discrepancies have been a factor between 2 and 10. The discrepancy depends on the quality of the measurements but also on the method used for the inversion procedure when the electron energy spectral information is derived. For the Pulsaur II experiment we have used a method developed from the results found by Seltzer and Berger [1974] and Walt et al. [1979] to derive electron spectra from the X rays, and the results from Mæhlum and Stadsnes [1967] to convert the highly anisotropic electron fluxes into comparable equivalent isotropic electron fluxes. By using this method we obtained agreement well within the statistical errors of the measurements [Østgaard et al., 1998, hereafter called Paper 1]. For the PIXIE experiment we have used a look-up table provided by a coupled electron photon transport code originally developed to model the neutral particle transport [Lorence, 1992]. The coupled electron photon transport code was developed by Lockheed-Martin Advanced Technology Center and they have provided the look-up table used in our studies. This look-up table will hereafter be referred to as the look-up table provided by the code developed from the transport code by Lorence [1992]. Using this method we have obtained agreement within a factor of ~2 comparing electron energy fluxes and profiles of X rays [Østgaard et al., 1999b, hereafter called Paper 5].

To describe the production of X rays from the electrons entering the atmosphere we will shortly describe the two models used in our studies and a simplified method for calculating X-ray production analytically. In Figure 4 we have shown a typical X-ray spectrum resulting from an electron beam hitting a target. Both the emission lines depending on the atomic properties of the target and the continuous bremsstrahlung emissions are clearly seen. The atmospheric line emissions which are relevant for the incoming energetic electrons are listed in Table 4, but as we do not detect X rays below ~3 keV only the line emission from Ar must be taken properly into account when energy analysis is to be made. Even though the Ar contents of the atmosphere is very low (0.93% in volume or 1.28% in weight, up to 90 km) the contribution from this line has been thought to produce a peak in the measured bremsstrahlung spectrum. Luhmann and Blake [1977] calculated the intensity ratio of the K-α line emission to the bremsstrahlung in a 100 eV band, and found it to be 200-250%, which corresponds to 20-25% in a 1 keV band that is the energy resolution of the PIXIE measurements. However, they neglected the energy degradation of electrons and assumed the Ar content of the atmosphere to be a constant fraction of the N_2 content at all altitudes, which is not correct. Motivated by the energy analysis of PIXIE data a rerun of the codes using a more realistic Ar height profile and including the energy degradation of electrons, resulted in ratios of 4-8% for the PIXIE measurements (J. Luhmann private communication, 1998). We therefore consider the atmospheric Ar line emission to be negligible relative to the X-ray bremsstrahlung. As Ar is often used as stopping gas in proportional counters, e.g., PIXIE, the Ar lines still have to be considered (see Østgaard et al. [1999a], hereafter called Technical Report). Disregarding the line emissions of X rays for the moment, the continuous X-ray spectrum which is called X-ray bremsstrahlung (or white X rays) can be represented by (1) [Kulenkampff, 1922]

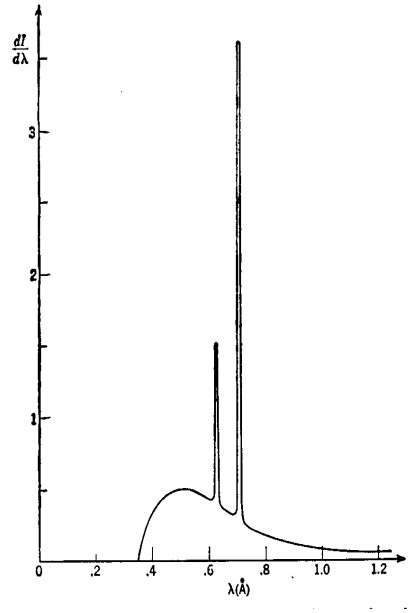

Figure 4. Typical energy spectrum for X rays, resulting from a monoenergetic electron beam hitting a target [Leighton, 1959].

Table 4. Emission lines given in keV for the main species in the atmosphere [Storm and Israel, 1967].

Species (Z)	K-L_{II}= α_2	K-L_{III}=α_1	K-M_{IIII} = β_3	K-M_{III} = β_1
Nitrogen (7)	0.393	0.393		
Oxygen (8)	0.524	0.524		
Argon (18)	2.956	2.958	3.191	3.191

$$\frac{dE_X}{d\nu} = C[Z(\nu_m - \nu) + 0,0025Z^2] \quad (1)$$

where $dE_X/d\nu$ is the number flux of X rays within the frequency interval, $d\nu$, ν_m is the frequency of the incoming electron (E_e/h) and determines the upper frequency of X rays that can be produced, Z is the atomic number of the atmosphere and C is a constant. This is known as the thick target semi-empirical approach which is qualitatively illustrated in Figure 5. When the production of X rays is determined, the propagation of X rays must be handled correctly, which includes the effect of photo-absorption, energy reduction and scattering (Compton and Thomson scattering).

In a realistic model of X-ray production the scattering of elec-

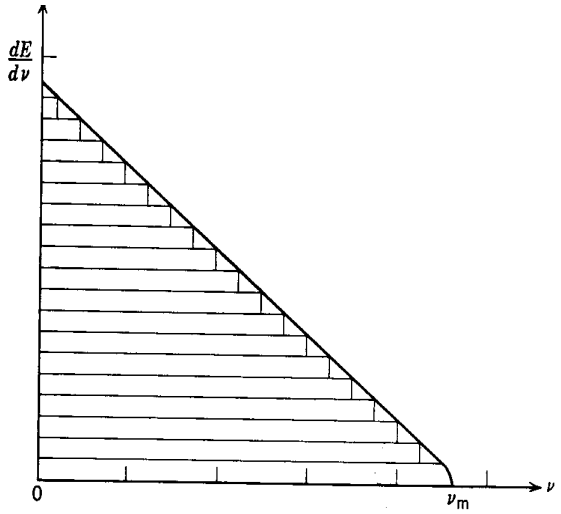

Figure 5. A qualitative representation of the X-ray bremsstrahlung spectrum according to the analytic formula from [Kulenkampff, 1922] (Figure from Leighton, [1959]).

trons, i.e., backscattering, Coulomb scattering and 'knock-on' scattering must also be included. Both the model by Berger and Seltzer [1972] and the code developed from the transport code by Lorence [1992] have included the processes mentioned above. (Berger and Seltzer [1972] has not included the elastic scattering of X rays, i.e., the Thomson scattering, as their model only deals with X rays >10 keV). They both have assumed an isotropic flux of electrons entering at the top of the atmosphere, but while the Monte Carlo model developed by Berger and Seltzer [1972] and Seltzer and Berger [1974] only has estimated the isotropic flux of X rays in the upward hemisphere, the code developed from the transport code by Lorence [1992] also provides the angular distribution of X rays in 10˚ intervals. This difference of precision is related to the use of different cross sections for the generating of X rays. While the former has used a cross section given by Sauter [1934] with a correction factor developed by Elwert [1939], the latter has used the same cross section but a correction factor developed by Elwert and Haug [1969]. By using this updated correction factor the angular distribution of X rays can be handled more properly (for more details, see Tseng et al. [1979]). In order to minimize this shortcoming of the Berger and Seltzer [1972] code in our Pulsaur II study, we used the results from another model developed by Walt et al. [1979] that gives us estimates of the angular X-ray distribution. Both the models [i.e., Berger and Seltzer, 1972; Lorence, 1992] provide look-up tables of X-ray production from electrons having an exponential energy spectrum (the code developed from Lorence [1992] also provides look-up tables of X rays from Maxwellian electron spectra). In Figure 6 the X-ray spectra generated by an electron exponential spectrum with an e-folding energy of 100 keV is shown for 8 different emitting angular intervals. Given these look-up tables it is possible to derive both single exponential and double exponential electron spectra from the X-ray measurements. Figure 6 illustrates that the energy range of X rays has to be considered when the e-folding energy of the X-ray spectrum is determined. In our algorithms we have identified two e-folding energies for every spectrum, one for the high energy range and one for the low energy

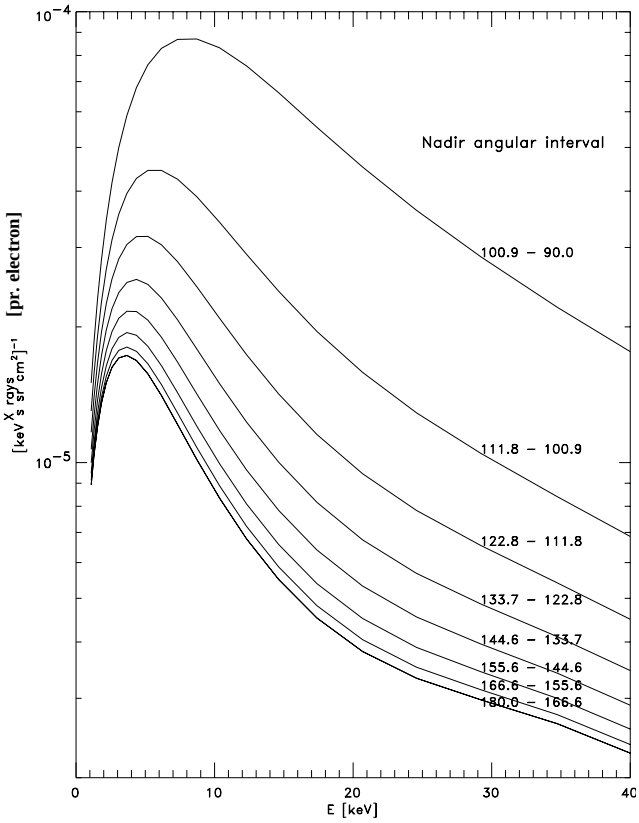

Figure 6. X-ray spectra calculated by the code developed from the transport code by Lorence [1992]. Here are shown the X rays emitted at 8 different nadir angular intervals (i.e., the upward hemisphere) from an electron exponential spectrum with an e-folding energy of 100 keV. The X-ray spectra are normalized to an integral flux of one electron. Both the angular distribution of X-ray emissions and the effect of escaping at slant angles from a plane atmosphere are taken into account.

range.

As the X-ray spectra from exponential electron spectra are found to have an approximately exponential shape, Robinson et al. [1989] have developed a simplified method to calculate a two parameter characteristic of the electron energy spectrum from the X-ray spectrum. This is a rather rough assumption as the X-ray spectrum most often must be fitted by different e-folding energies in the low- and high-energy range of X rays (see Figure 6). Assuming isotropic electron fluxes and single exponential electron energy spectra they obtained quasi-analytic expressions for how the characteristic energies of the electrons and X rays are coupled (2).

$$E_{0X} = \frac{18E_{0E}}{18 + E_{0E}} \tag{2}$$

Then the electron energy flux Q_E was found to be coupled to the X-ray flux, $F(K)$ and a efficiency function $g_1(K)$ given by (3), when $g_1(K)$ is expressed as (4). K is the X-ray energy.

$$F(K) = g_1(K)Q_E e^{(-K)/E_{0E}} \tag{3}$$

$$g_1(K) = 1.96 \times 10^{-5} K^{-1.9} \quad (4)$$

By using the results from Walt et al. [1979] they also found an expression for the angular distribution of the X rays related to the X-ray flux at 180˚ given by (5), restricted to E_{0E}< 20 keV and θ>100˚.

$$\Phi(K, E, \theta) = \Phi(K, E, \theta = 180°) \times \left(\frac{-2}{\cos\theta} - 1 \right) \quad (5)$$

These expressions may be regarded as rough estimates of the X-ray spectra from electrons (or vice versa) and it should be emphasized that neither the X-ray spectrum nor the electron spectrum can always be properly represented by single exponentials. From both previous studies and the papers in this thesis we know that the X-ray spectra can be well represented by either single or double exponentials [Barcus and Rosenberg, 1966; Goldberg et al., 1982; Paper 1; Paper 5]. A double exponential is defined by

$$j(E) = j_{01} e^{-E/E_{01}} + j_{02} e^{-E/E_{02}} \quad (6)$$

where j_{01} and j_{02} are the flux at zero energy and E_{01} and E_{02} are the two e-folding values. In [Paper 1, Paper 5] we also found that the electron spectra can be represented by single or double exponentials, but sometimes Maxwellian or a Kappa function would probably be more suitable [e.g., Sharber et al., 1998].

For the inversion techniques based on X-ray measurements we may conclude that it is possible to obtain a 4-parameter characteristic of the electron precipitation, giving information about both the low-energy and the high-energy range of electrons, which none of the other remote sensing techniques are able to provide.

2.4. Summary on remote sensing techniques

Our Table 5 is a copy of Table 3 from the paper of Robinson and Vondrak [1994], which has a more detailed discussion of the imaging techniques than presented here, and we let this table summarize the discussion of the different remote sensing techniques. However, regarding the evaluation of the UV imaging technique the authors seem to have been too optimistic about the ability to obtain images both at daytime and nighttime. Even though the albedo of UV emissions (<1700 Å) is negligible there is a significant contamination from sunlight generated UV emissions (dayglow)[G. Germany private communication, 1999]. Thus the UV imaging is most successfully provided during night time. We may therefore conclude that X-ray imaging is the only imaging technique that can be successfully utilized even in the sunlit part of the ionosphere. Furthermore, as X-ray measurements enable us to extract multi-parameter information about the parent electron spectrum this technique is favourable in estimating the total energy input into the ionosphere during substorms and storms. However, when studying fine structures of auroral features both the visible and the UV imaging techniques are more suitable. Due to the small amount of X-ray photons produced, X rays must be integrated over relatively wide areas to achieve good statistics. Thus the combined use of the different imaging techniques would provide the ultimate tools to study both fine structures and energy deposition into the atmosphere.

Table 5. Comparison of remote sensing methods (Table 3 in Robinson and Vondrak [1994])

	X rays	UV	Visible
Temporal coverage	Day and night	Day and night	Night only
Albedo correction	Unnecessary	Unnecessary	Needed
Absorption correction	Usually unnecessary	Often necessary	Usually unnecessary
Emission processes	Well understood	Somewhat understood	Somewhat understood
Atmospheric background	Negligible	Negligible	Sometimes significant
Derivation of geophysical parameters	Straight-forward	Chemistry-dependent	Chemistry-dependent
Electron spectral information	Multi-parameter	Two-parameter	Two-parameter
Characteristic electron energy sensitivity	1-100 keV	<10 keV	<10 keV
Validation	Proven	Proven	Proven

3. Previous studies of energetic electron precipitation

Due to the lack of global imaging instruments of the energetic electron precipitation in the past (see Table 2), our knowledge of this part of the substorm has been based on measurements of cosmic radio noise absorption by riometer [e.g., Hartz and Brice, 1967; Jelly and Brice, 1967; Berkey et al., 1974], X-ray measurements from balloon campaigns [e.g., Barcus and Rosenberg, 1966; Bjordal et al., 1971; Kangas et al., 1975], particle measurements in space [e.g., McDiarmid et al., 1975; Hardy et al., 1985; Codrescu et al., 1997] and X-ray measurements from low-altitude satellites [e.g., Imhof et al., 1980; Chenette et al., 1992]. In this section we will briefly report some of the results from these previous studies which are relevant for the discussion of our findings from PIXIE data. We will focus on studies that have revealed information about the global features of energetic precipitation either statistically [e.g., Hartz and Brice, 1967, McDiarmid et al., 1975] or by studying isolated substorms [e.g., Berkey et al., 1974, Sletten et al., 1971]. We will also present some studies on the dynamics in the source region of the auroral particle precipitation, i.e., the injection of electrons during the early expansion phase of the substorm [Reeves et al., 1991, Birn et al., 1998].

3.1. Cosmic radio noise absorption

From about the 50s' the technique of determining particle precipitation indirectly from enhanced absorption of cosmic radio noise was developed. The basic concept of this technique is that the incoming cosmic radio noise intensity (I_0) will be attenuated when entering the ionosphere as a function of depth, because the absorption coefficient, κ is altitude dependent. The intensity of cosmic radio noise (I) at a given altitude is then given by

$$I = I_0 e^{-\int_{h_1}^{h_2} \kappa(h)dh} \tag{7}$$

Due to the Appleton-Hartree equation, κ is given by

$$\kappa(h) = C \cdot \frac{N_E(h)\nu_E(h)}{\nu_E(h) + (\omega \pm \Omega_E(h))^2} \tag{8}$$

where C is a constant, N_E is the electron density, ν_E is the collision frequency between electrons and neutral particles, Ω_E is the electron gyro frequency and ω is the frequency of the actual cosmic radio noise. When measuring cosmic radio noise at 30 MHz, both ν_E and Ω_E are negligible comparing to ω and κ becomes approximately proportional to the product of N_E and ν_E. As ν_E rapidly falls off due to the rapid decrease of the density of the neutral atmosphere, the absorption of cosmic radio noise is usually not very significant above ~100 km, i.e., at the altitude of maximum 10 keV electron energy deposition [e.g., Rees, 1963]. This implies that most of the absorption occurs at altitudes (<100 km) were electrons in the energy range from 10 to 100 keV deposit their energy [Berkey et al., 1974]. However, for large electron fluxes with a very soft spectrum even electrons down to 5 keV will contribute significantly to the total absorption [Barcus, 1965]. Keeping this in mind, we conclude that the riometer data provides information mainly about the energetic particle precipitation.

Cosmic radio noise absorption correlated with other measurements have been used to construct characteristic average features of precipitation and to study the dynamics of the energetic electron precipitation during substorms. By using the results from several years surveys of all-sky data, 5577 Å emission features, riometer data, ionosonde data, X-ray measurements from balloons and in-situ particle measurements Hartz and Brice [1967] constructed diagrammatically the average precipitation features of the soft (triangles) and the energetic (solid dots) electrons (Figure 7). They found that the soft electron precipitation was related to the auroral oval while the energetic electron precipitation constituted the auroral zone. These two regions were found to overlap in the midnight region but at all other local times the auroral zone, associated with the diffuse aurora is equatorward of the auroral oval. This result has important implication on the source location of the different electron energies in the magnetosphere. In the region where substorm onset on the average takes place, i.e., around midnight, both the soft and energetic precipitation occur at about the same latitudes at field lines that are connected to the near-Earth central plasma sheet (CPS). At dawn, day and dusk the soft electron precipitation is associated with field lines very close to the open-closed boundary, while the hard drizzle precipitation is associated with field lines well within the stable magnetosphere. They found two local time maxima of precipitation, one pre-midnight (mostly soft but also energetic electron precipitation) and another between dawn and noon (only energetic electron precipitation). As

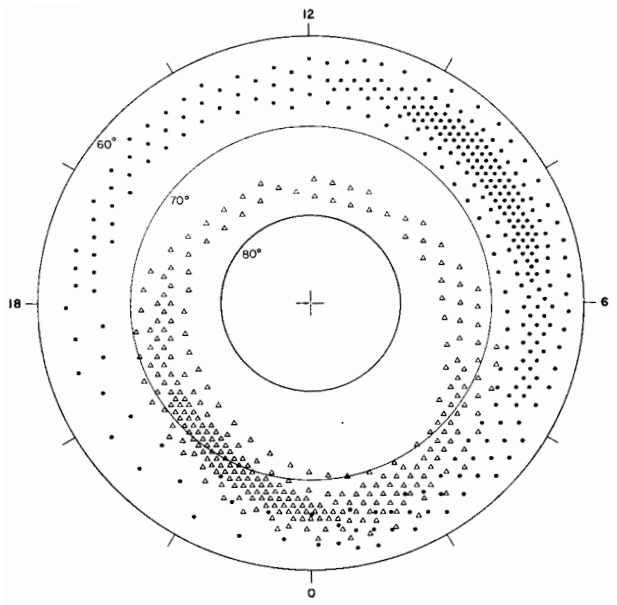

Figure 7. An idealized representation of the two main zones of auroral particle precipitation the northern hemisphere, where the average intensity of the influx is indicated very approximately by the density of symbols on a geomagnetic grid. Triangles show the soft electron precipitation and the dots show the energetic electron precipitation. (Same as Figure 19 from Hartz and Brice [1967]).

they used large averaged data sets, the various features could not be interpreted in the context any substorm evolvement.

Jelly and Brice [1967] utilized the electron measurements (>40 keV) from the Alouette 1 satellite crossing through the dawn-noon region, combined with magnetometer data close to the substorm onset region at midnight and cosmic radio noise absorption data from stations in the morning sector to examine how the dawn to noon maximum of energetic precipitation was related to the substorm onset at midnight. They found a clear indication that nighttime substorms and morning diffuse precipitation are strongly associated and that the probability of the latter to occur, delayed to substorm onset, increased provided it followed a moderately disturbed period even if the substorm onset itself was weak or moderate. They related this to the concept of a maximum stable limit for fluxes of trapped energetic electrons suggested by Kennel and Petscek [1966] and found that the time delay between onset in morning sector relative to the substorm onset time corresponded to the drift time of ~40 keV unstably quasi-trapped electrons.

One of the most extensive studies based on riometer data has been performed by Berkey et al. [1974]. By initiating a large collaboration among 6 different groups, 40 riometer stations were used to study 60 substorms during solar minimum (1964-1965) and solar maximum (1969). Even though there was a lack of stations in the Atlantic along the auroral zone, introducing some uncertainties, they were able to draw isocontours of absorption between the 40 stations to obtain the temporal development of isolated substorms with a time resolution of 15 min. In Figure 8 we have shown their average substorm obtained from all the 60 substorms studied. Substorm onset (T=0000, i.e., hhmm) was found to occur (on average) around midnight, expanding into the morning sector (T=0015) and about T=0030 a maximum of absorption appears in the morning sector at ~6 MLT and continues for ~2

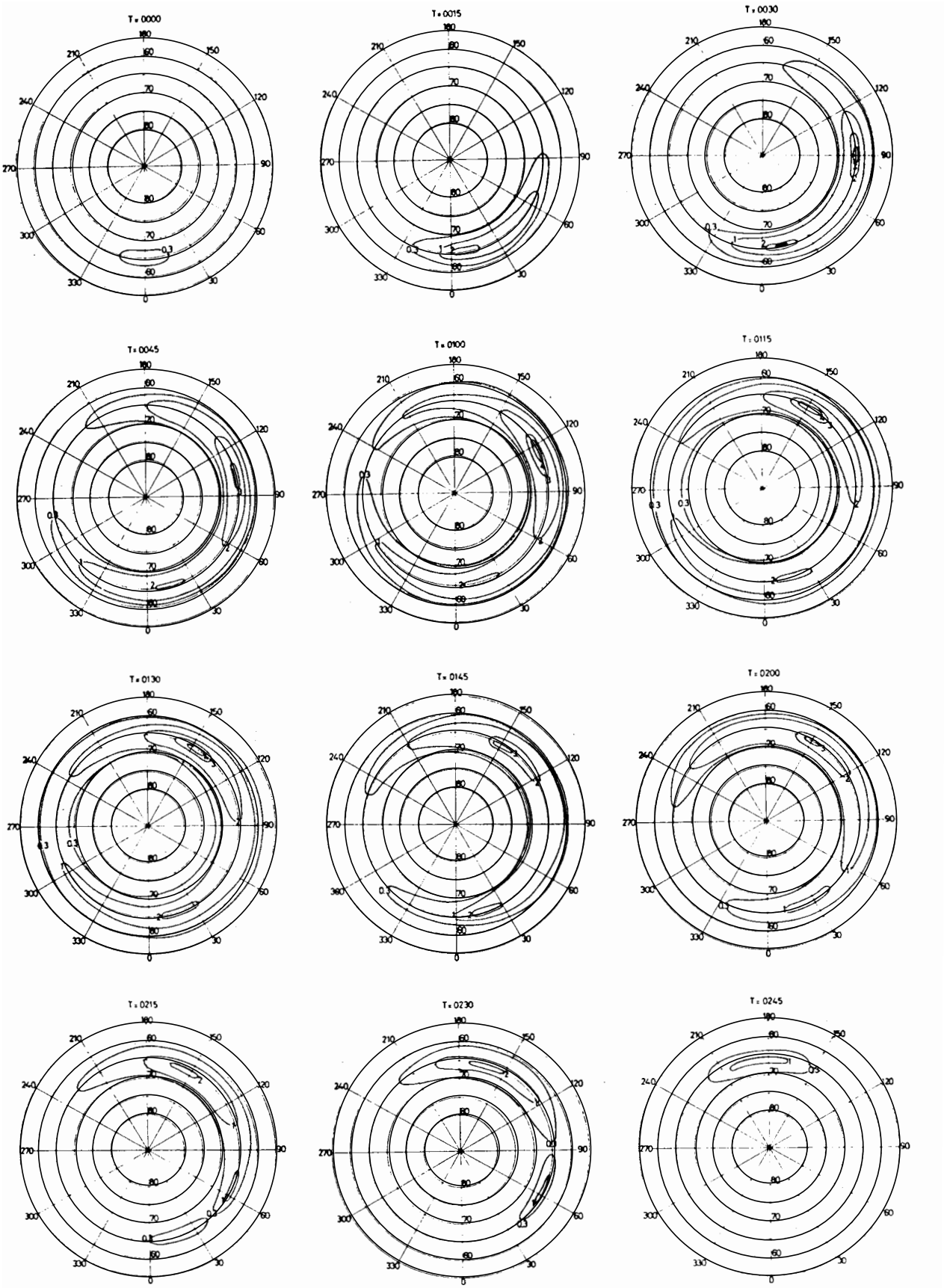

Figure 8. Average substorm picture obtained from 60 substorms by drawing isocontours of cosmic radio noise absorption. The time resolution is 15 min and CGM grid is used (same as Figure 9 in Berkey et al., [1974]).

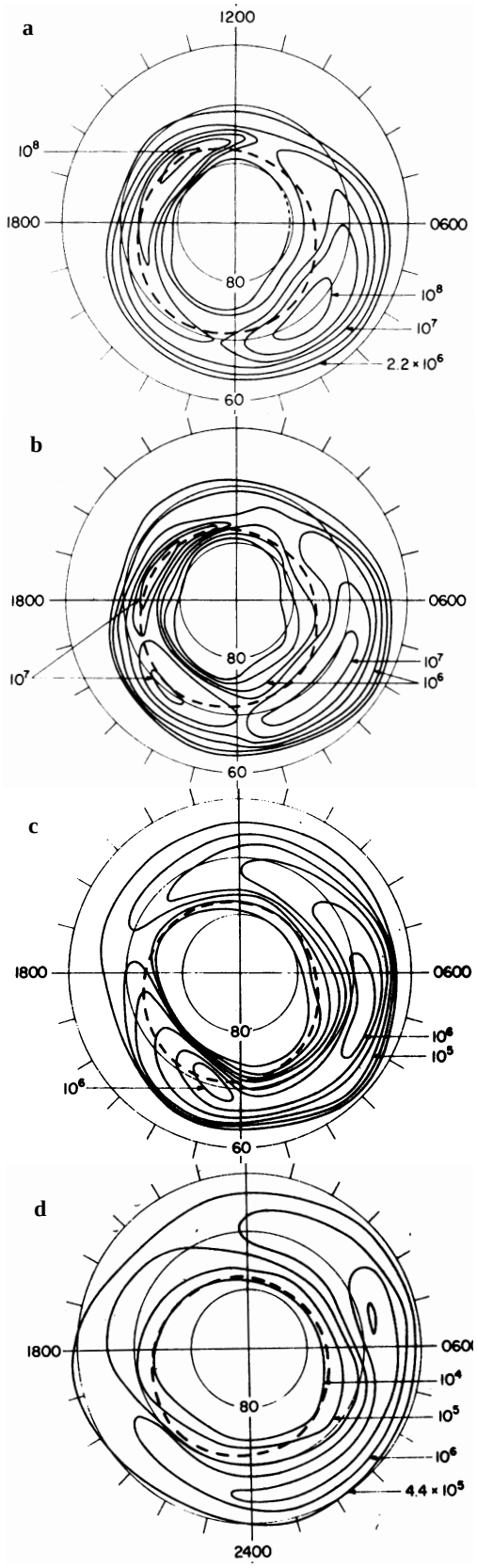

Figure 9. Average intensity contours for electrons of (a) 150 eV, (b) 1.3 keV, (c) 9.6 keV and (d) 22 keV given as $(cm^2\ s\ sr\ keV)^{-1}$ for Kp <3 and pitch angles <45°. CGM grid is used for all plots with noon at the top. (Same as Figures 4, 6, 8 and 9 from McDiarmid et al. [1975]).

hours, with the peak of absorption slowly moving towards noon. In almost every substorm they found an eastward expansion with velocities independent of magnetic activity (i.e., the Kp index) and for most substorms this expansion corresponded to the magnetic curvature and gradient drift of electrons in the energy range ~50-300 keV. However, for some cases they found extreme velocities that corresponded to ~1 MeV, but most likely this must be explained by some injections they missed due to the scarce density of stations in some regions. The eastward velocities they found showed a clear tendency of slowing down at the dayside of the Earth, which is consistent with a magnetic field configuration compressed at the dayside and stretched down the tail giving a much larger magnetic gradient at nightside than dayside. Westward expansion, often associated with the westward travelling surge (WTS) was found in less than half of the substorms expanding occasionally either along the auroral oval or the auroral zone, indicating that this feature is not a common part of the energetic precipitation morphology during substorms. The velocities found for the equatorward and poleward expansion increased from ~0.5 km s^{-1} to 1.0 km s^{-1} depending on the Kp index and were found to be in good agreements with previous results [e.g., Akasofu et al., 1966]. We should also notice that they did not report any increase in absorption when the stations entered the sunlit hemisphere. Thus they found no evidence for the morning maximum to be caused by any increase of cold plasma density diffusing from the upper atmosphere into the magnetosphere and causing increase of precipitation of energetic trapped electrons, as proposed by Brice and Lucas [1971]. This is probably because the sunlight is entering the atmosphere at very slant angles at these high latitudes and the effect, if any, will be smoothed.

3.2. Particle studies

In-situ measurements of electrons at low altitudes and throughout the magnetosphere have been widely used in substorm studies during the last three decades. Here we will pay attention to one of the early statistic studies on the morphology of energetic electrons and some of the studies based on electron measurements at geosynchronous orbits in order to study injection fronts, drift and energization of electrons in a modelled magnetic field.

3.2.1. Morphological Studies.

From large data sets from low-altitude satellites it is possible to construct average contours of precipitating electrons for different energies. Hardy et al. [1985] used the data set from the Defense Meteorological Satellite Program (DMSP) satellites to study electrons in the energy range from 50 eV to 30 keV and Codrescu et al. [1997] constructed maps of average flux in the energy range from 30 keV to >300 keV using the National Oceanic and Atmospheric Administration (NOAA) satellites. As the satellites used for these two studies were all launched into sun-synchronous orbits some local times in the afternoon and post midnight sector were not covered, introducing some uncertainties into their results. The European Space Research Organisation 1 Aurorae (ESRO 1A) satellite provided better coverage and some results of the average fluxes of precipitating (i.e., at ~10° pitch angles) electron energies of 1 keV, 6 keV and 13 keV for 4 different magnetic activity level ($Kp=0^0$-1^0, 1^+-3^0, 3^+-5^0 and 5^+-9^0) have been presented by Riedler and Borg [1972]. McDiarmid et al. [1975] based their study on ISIS-2 data, and as this satellite precessed ~4 min/day they obtained a complete local time coverage in about 5 months. The instruments measured electrons in the energy range from 150 eV to >210 keV. Measurements from ~1100 passes in the northern hemisphere were grouped according to electron energies into 1°

invariant latitude intervals, 2 hour MLT intervals, three pitch angle intervals and several ranges of Kp. To exclude large storm data only passes during Kp < 3 were used to obtain average intensity contours for different electron energies. Figure 9 is a composition of 4 of the figures from their paper, showing contours of 4 different electron energies for Kp <3 and pitch angles <45°. For the low-energy electrons (150 eV, shown in Figure 9a) two maxima can be seen, one in the post-noon and another in the post-midnight sector, which they related to cleft electrons or magnetosheat electrons entering the closed field region at these local times. For electrons at 1.3 keV (Figure 9b) the two maxima are still significant, but a third maximum appears in the pre-midnight sector related to substorm breakup events. Going further up in energy, Figure 9c shows the intensity contours for 9.6 keV electrons. Now the two soft electron maxima have disappeared but the pre-midnight maximum is still apparent. For electrons at this energy a second maximum is found in the morning sector and for even higher electron energies, 22 keV in Figure 9d, only the morning maximum remains. They related this high energy morning maximum to the drift of electrons and some precipitation mechanism that was believed to be most efficient in the morning sector.

3.2.2. Substorm Particle Injections and Drift Paths of Injected Electrons.

As mentioned above the ionospheric features of electron precipitation are related to a source location in the magnetosphere. Even though there are still a lot of unresolved issues connected to our understanding of the evolvement of substorms, some basic concepts seem to be commonly accepted. Prior to the substorm onset a growth phase [McPherron et al., 1973], associated with the merging of the interplanetary magnetic field (IMF) at the subsolar magnetosphere due to the southward turning of the IMF, accomplishing a more efficient coupling and energy transport from the solar wind into the magnetosphere. During the growth phase the magnetotail becomes stretched due to the strengthening and thinning of the cross tail currents and the CPS [Kokubun and McPherron, 1981; Pulkkinen, 1991]. Furthermore, increased directly driven precipitation at dawn, day and dusk [Elphinstone et al., 1991] and a brightening at the equatorward edge of the diffuse aurora at midnight [Sergeev et al., 1983] are very often observed. As a consequence of the very stretched magnetic field and the thinning of the current sheet which unstabilize the system, the formation of a near-Earth neutral line (NENL) through a reconnection process [Hones, 1976; Hones, 1977; Hones, 1979; Shiokawa et al., 1998] is believed to occur. The rapid change of the magnetic field caused by the reconnection process leads to an induced electric field which will increase the convective drift of particles towards the Earth. This abrupt increase of convective drift or commonly called the dispersionless injection of particles have been widely studied by geosynchronous satellites [e.g., Reeves et al., 1990]. Then it has been proposed that the braking of the particles in the near-Earth CPS is what initiates the field-aligned currents, the current wedge formation and dipolarization of the magnetic field lines related to the breakup of the substorm onset [Rostoker and Eastman, 1987; Shiokawa et al., 1998]. This defines the beginning of the substorm expansion phase. Throughout this phase and the recovery phase the injected particles will drift due to the forces of the magnetic and the electric field.

This very short description of the substorm evolvement is meant to introduce the injection process, which have been used to determine the substorm onset time [e.g., Erickson et al., 1979; Østgaard et al., 1999c, hereafter called Paper 2; Håland et al., 1999, hereafter called Paper 3] and the subsequently drift of electrons during the expansion phase and throughout the recovery phase [Reeves et al., 1990; Reeves et al., 1991; Friedel et al., 1996]. From particle measurements from geosynchronous satellites both the injection signatures and the dispersed drift signatures have been thoroughly examined. Here we will refer to Friedel et al. [1996], who examined one year of Combined Release and Radiation Effects Satellite (CRRES) data to determine dispersionless injection signatures in order to find the most probable location for the injection to occur. The orbit of the CRRES satellite was close to the equatorial plane with the apogee at L=8.1 wandering from 8 MLT to 16 MLT throughout its lifetime. This paper reports that dispersionless injection signatures were observed at distances from L=4 to L=7, with a peak occurrence frequency at L=~6. They also found the ion injection to occur most frequently in the post midnight region at 24-03 MLT while the electron injection had a peak occurrence frequency around 21-23 MLT.

In the paper of Reeves et al. [1991] the curvature and gradient drift of energetic particles were numerically modelled. To model a realistic magnetic field a model by Tsyganenko and Usmanov [1982] was used. In order to calculate the gradient and curvature drift for all pitch angles they used the invariant integral (2. adiabatic invariant) given by

$$I = \int_{m_1}^{m_2} \left[1 - \frac{B(s)}{B_M}\right]^{1/2} ds \tag{9}$$

where $B(s)$ is the magnetic field strength along the field line, B_M the magnetic field strength at the mirror points, m_1 and m_2. The bounce average drift velocity, v_D is then given by

$$v_D = \langle v_{GC} \rangle = \frac{2W}{qS_B B_0} \nabla_0 I \times \hat{\mathrm{B}}_0 \tag{10}$$

where W is the kinetic energy, q is the charge and subscript 0 denotes values at the equator and S_B (11) is the so-called half-bounce path length.

$$S_B = \int_{m_2}^{m_2} \left[1 - \frac{B(s)}{B_M}\right]^{-(1/2)} ds \tag{11}$$

By using these equations together with the magnetic field model, they simulated the drift velocities for different particle energies at different pitch angles. The derived drift velocities showed about a 30% decrease from midnight to day, due to the changes in magnetic gradient, which was also seen in the figures from Berkey et al. [1974]. By using the information of the dispersed drift echoes seen at geosynchronous orbit the numerical model was used to trace back in time the location of the dispersionless injection. Using measurements from 3 of the Los Alamos National Laboratory (LANL) satellites Reeves et al. [1991] estimated both the injection regions for electrons and protons, their location and time of arrival. Figure 10 shows the schematic representation of the injection region for both electrons and protons using both local measurements (spacecrafts A and B) and the remote determination from spacecraft C and the drift model (same as Figure 16 from Reeves et al. [1991]). As can be seen they inferred a region called the central injection region of both electrons and protons and an dawnward electron periphery and a duskward proton periphery. The two peripheries result from the

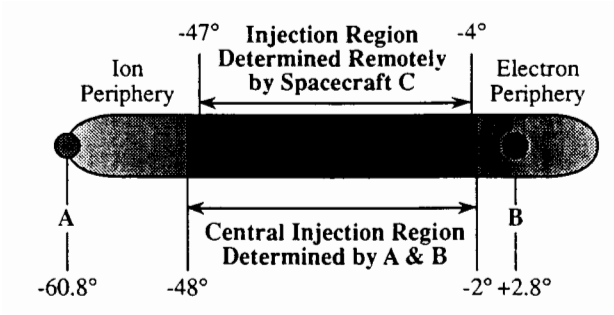

Figure 10. A schematic of the comparison between local measurements of the injection region from spacecraft A and B, and remote determination of the injection region using observation from spacecraft C and the drift model (same as Figure 16 from Reeves et al. [1991]). The extension of the injection regions are indicated by geomagnetic longitudes relative to midnight.

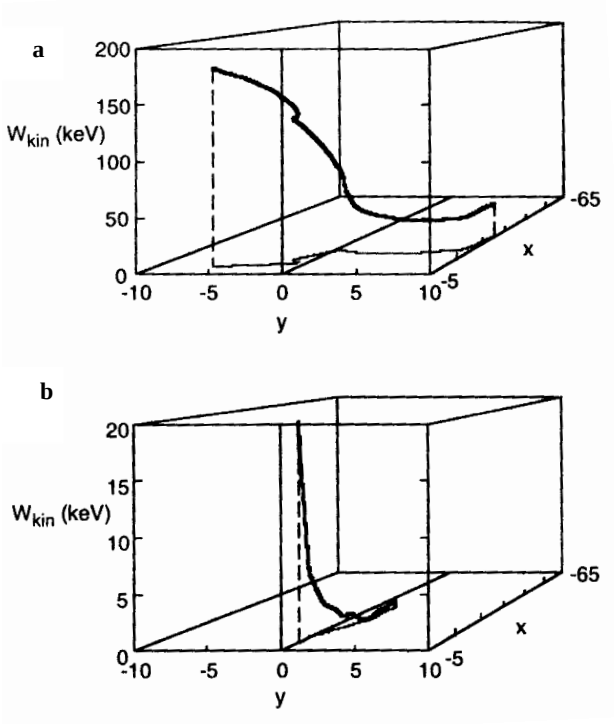

Figure 11. Energy variations of sample electrons that end at x=-10 R_E and y=0 R_E at t=7 min. The figures show the trajectories for electrons that are energized from the reconnection region at x=-23 R_E up to: (a) a final energy of 180 keV; (b) a final energy of 20 keV. They illustrate that most of the energy gain occurs during the earthward drift in the collapsing inner tail (same as Figure 11 from Birn et al. [1998]).

curvature and gradient drift which is opposite directed for electrons and protons.

Birn et al. [1998] have modelled the injection trajectories for different electron energies due to the collapse of the magnetic field during the reconnection process. The reconnection process leads to an induced electric field which determines the injection and as the curvature and gradient forces act differently on electrons at different energies, their trajectories are quite different. This is illustrated in Figure 11 (same as their Figure 11) showing the trajectories for electrons that are energized from the reconnection region at x=-23 R_E up to energies of 180 keV and 20 keV at x=-10 R_E and y=0 R_E. When observing both particles at midnight at x=-10 R_E it can be seen that the 180 keV electron has drifted in from the flank of the magnetosphere while the 20 keV electron has drifted in the CPS close y=0 R_E all its way from the reconnection region. Thus, if the electrons at different energies have a source region in the distant tail with a small azimuthal extension an energy structured injection region would be observed, with an eastward displacement of the injection region for the higher energies. Another result from this paper which should be mentioned is that the strongest electric field induced by the reconnection process appears around x=-15 R_E even if the reconnection region is a x=-23 R_E. The results from comparisons with measurements makes this model rather convincing.

3.3. Balloon campaigns

From 1960 and 1970 a large number of balloon campaigns were performed. Scintillators and Geiger-Müller tubes flown at balloon altitudes (~35 km) provided X-ray measurements which were compared with different ground based measurements like magnetometers and absorption of cosmic radio noise. From 53 balloon flights Barcus and Rosenberg [1966] studied the temporal and spectral variations of X rays at almost all local times. The main results from their study are shown in Figure 12, a polar plot showing increasing e-folding energies from the center and outward with midnight at the bottom and noon at the top. Starting from pre-midnight the sporadic nigh time activity, related to substorm onset events have a large range of e-folding energies. Moving to the early morning slowly varying bay events of hard X rays and fast pulsations with softer X-ray spectra are shown. Close to noon microbursts (50 ms) with hard spectra were observed. Such microbursts have been observed by others in the midnight region as well [e.g., Parks et al., 1968]. Bjordal et al. [1971] studied the X-ray events in the midnight sector and found them to correlate very well with ground based magnetic bay signatures. They also found that the X-ray spectra showed an abrupt hardening at the substorm onset with a subsequently softening. Pytte and Trefall [1972] have reported significant growth phase signatures of enhanced X-ray emissions, $^1/_2$ - 1 hour before substorm onset. The spectra observed during such events were interpreted to be consistent with adiabatic heated electrons, i.e., electrons drifting towards the Earth in an increased convective electric field.

By using riometers and magnetometers from Canada stations combined with balloon launches from Scandinavia, the relation between the substorm onset and the slowly varying events in the morning sector were studied [e.g., Sletten et al., 1971; Kangas et al., 1975]. In Figure 14 we show one of the figures from Kangas et al. [1975] where the cosmic radio noise absorption was measured (July 28, 1965) at Great Whale River (L=6.9) and the X rays were measured with two Geiger-Müller tubes flown on a balloon from Andenes (L=6.3). One of the Geiger-Müller tubes had walls of Al and the other had an internal Bi screen, giving a higher low-energy threshold for the latter and thus the ratio of the measured X-ray intensity from the two tubes could be used to extract spectral information. The bottom panel shows the spectral development through the event at Andenes with a double structure, i.e., the two peaks of hardening of the spectra correspond to two pulses of injected electrons at midnight during the substorm expansion

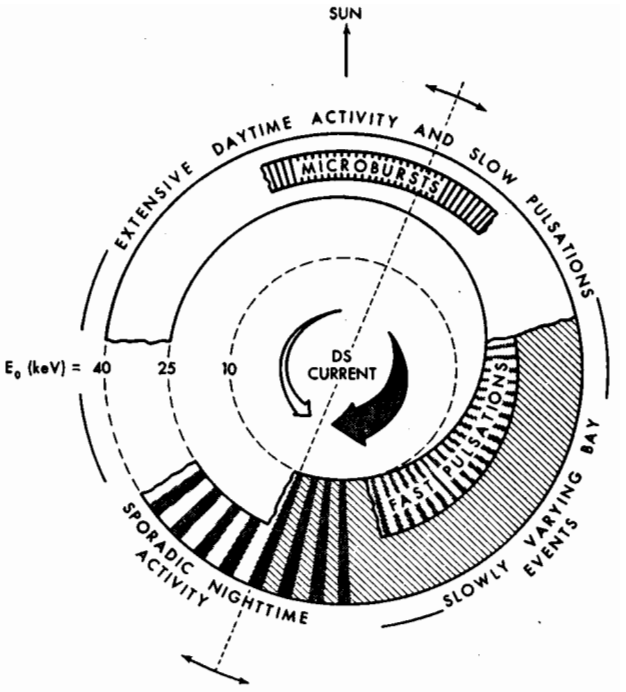

Figure 12. Diurnal pattern of the spectral character of energetic (~50-250 keV) electron precipitation suggested by bremsstrahlung X-ray observations in the auroral zone [Barcus and Rosenberg, 1966].

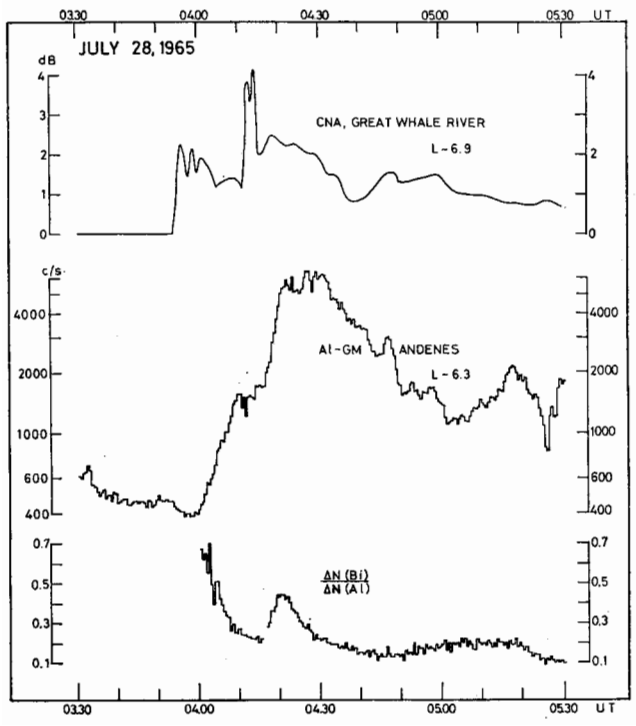

Figure 13. X-ray recordings in Scandinavia on July 28, 1965 and simultaneous riometer recordings from the midnight sector from Great Whale River [Kangas et al., 1975].

phase. The time delay from substorm onset to the onset of the slowly varying X-ray event in the morning were used to evaluate the drifting rain cloud model, i.e., electrons were injected at midnight and then drifting due to the curvature and gradient drift into the morning sector. By using the simple calculation of equatorial mirroring electrons in a dipole magnetic field [Lew, 1961] they found the time delays from 41 events to correspond with the expected drift time of electrons in the energy range 100-200 keV. In a similar study of 45 substorm events from 1963 to 1964 Sletten et al. [1971] used magnetometer measurements at local midnight to define the substorm onset time and X-ray measurements at balloon altitudes in the morning sector to define the onset time of the slowly varying X-ray events. They found the time delays to correspond to drifting electrons of ~140 keV.

3.4. Summary on previous studies

From the statistical studies based on in-situ electron measurements and riometer measurements there are found to exist two maximum regions of energetic precipitation but three maxima in the softer precipitation (~1 keV). Focusing on the energetic precipitation the first and most intense maximum is found to be situated around midnight and to be related to the injection of fresh electrons and another maximum to be located between dawn and noon, most probably related to the drifting electrons. However, by focusing on electron precipitation at lower energies (~1 keV), there is found to exist an additional maximum in the postnoon region. This region is also found to have an almost complete lack of X-ray emission [Petrinec et al., 1998]. Except for the study by Berkey et al. [1974] most of the studies were based on adding all the observed precipitation during different kinds of geomagnetic activity and providing no information on the temporal behavior of single substorms.

The time delays between the morning activity and the substorm onset in the midnight sector were found to be consistent with the drift of electrons of energies from ~140 keV [Sletten et al., 1971], 100 keV [Berkey et al., 1974] and 100-200 keV [Kangas et al., 1975].

Modelling of curvature and gradient drift velocities in a realistic magnetic field model has shown that the observed drift echoes seen at geosynchronous orbits can be used to infer information about the shape of the injection region, as well as the onset time of the injection. Furthermore, modelling of the energization of the injected particles caused by the reconnection process in the near-Earth magnetotail has revealed the observed shift of injection fronts for protons and electrons as well as particles with different energies.

4. Pulsaur II rocket experiment

Pulsaur II was a sounding rocket experiment, launched from Andøya Rocket Range (66.1˚ CGM latitude) at 23.43 UT (0130 MLT) on February 9, 1994, into a pulsating aurora during the recovery phase of a substorm. We utilized the X-ray measurements and electron measurements during this flight to develop and evaluate a method for deducing the energy spectrum of the electron precipitation from the X-ray measurements [Paper 1]. In this section we will describe in more detail some of the procedures used in that study and discuss the conclusions of the paper.

An X-ray detector measured X rays from 5.6 keV to >35.4 keV and a photometer measured at the 4278 Å emission line, looking at 135˚ and 150˚ relative to the spin axis of the rocket, respectively (see Figure 1 on page 30, Paper 1). We used the information from

an all-sky camera, combined with the correlation between pulsations in the X rays and the prompt N_2^+ emission to find the time interval best suited for comparing the electrons and the X rays (see Figure 3 and Figure 4 on page 32, Paper 1). We selected a time-interval when the footprint of the field line at the rocket position (i.e., the electron measurements) and the area of the X-ray measurements were close and both within a region of approximately spatial uniform precipitation.

The method used to derive the isotropic flux of electrons from the X-ray measurements was based on tables from Seltzer and Berger [1974] and Walt et al. [1979] as described in Section 2.3. The electron measurements were provided by an electrostatic analyser and a solid state detector and when making some assumptions [for details, see Paper 1] we obtained energy spectra from 10 eV to ~250 keV and full pitch angle information about the electrons from 10 eV to 25 keV. To be comparable to the isotropic electron precipitation in the downward hemisphere derived from the X-ray measurements we transformed the highly anisotropic measured electron distribution (see Figure 8 on page 36, Paper 1) into an equivalent isotropic distribution of electrons, by which we mean the isotropic flux of electrons that would result in the same number of absorbed electrons as the anisotropic electron flux will give. To do this we used the results from Mæhlum and Stadsnes [1967] to find the fraction of absorbed electrons entering the atmosphere at different nadir angles (θ). Contrary to earlier studies based on a secant-θ method [e.g., Rees, 1963] their Monte Carlo method did not give any altitude dependence of the maximum absorption peak for different nadir angles. However, they found the magnitude of energy deposition to decrease with increasing nadir angles as the fraction of backscattered electrons increases when entering at slant angles. Both methods are shown in Figure 14. From their Table 2.2. we found the fractions of absorbed electrons (i.e., the electron energy deposition efficiency) for 20 keV electrons, which are similar for 52 keV, 80 keV and 100 keV, at three different nadir angles, i.e., θ = 30˚, 60˚ and 80˚. We interpolating the fraction of absorption between these nadir angles. Then we calculated the total electrons entering a horizontal unit area of a plane atmosphere within 9 pitch angle intervals from 0˚-90˚ using (12). By setting the pitch angle equal to the nadir angle, which is a reasonable assumption at such high latitudes, we established the fraction of absorbed electrons in each 10˚ pitch-angle interval (A_i) given in Table 6. By using (13) we transformed the measured anisotropic electron directional fluxes j_{Mi} into an equivalent isotropic electron flux, j_{IS} (s sr keV cm^2)$^{-1}$, that would result in the same number of absorbed electrons as the anisotropic electron distribution will give.

$$J(\alpha_1 < \alpha < \alpha_2) = \pi((\cos\alpha_1)^2 - (\cos\alpha_2)^2) \qquad (12)$$

$$j_{IS} = \frac{\sum_{i=0}^{8} j_{Mi} A_i}{\sum_{i=0}^{8} A_i} \qquad (13)$$

To do this calculation properly the measured electron flux has to be transposed from rocket altitude down to 100 km, i.e., where the X rays are assumed to be produced. As this was not done in the calculation in Paper 1 we did also include electrons outside the loss cone in our calculation of an equivalent isotropic flux of electrons. However, we have rerun the calculations, transposed the fluxes within the loss cone at the rocket altitude (i.e., at pitch angles <74˚) down to 100 km according to Liouville's theorem and the conservation of the 1. adiabatic invariant. By looking into the codes once more we also found that the double exponential X-ray representation of the measured X-ray spectra were slightly overestimated. Correcting for both these errors we now obtain better fits for the X-ray spectra as can be seen in Figure 15 (which is

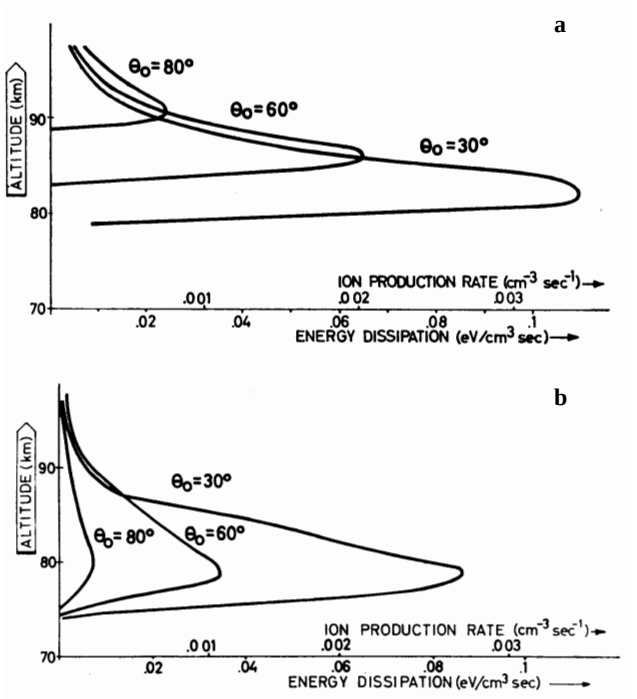

Figure 14. Production rate of ionization in the atmosphere for a non-vertical beam of monoenergetic electrons (flux = 1 electrons (cm^2 s)$^{-1}$) with E_0 =100 keV. (a) Calculation based on a secant-θ_0 correction (θ is the nadir angle) in the atmospheric depth. (b) Calculation based on Monte Carlo-method. (same as Figure 4.2 and Figure 4.6 from Mæhlum and Stadsnes [1967]).

Table 6. Values for estimating the equivalent isotropic flux of electrons from anisotropic electron fluxes.

Pitch angle interval i=(α_1-α_2)	J(α_1<α<α_2)	Fraction absorbed [Mæhlum and Stadsnes, 1967]	Absorbed electrons (A_i)
0 = 0 -10	0.0947308	0.86	0.0814685
1 = 10 - 20	0.272766	0.85	0.231851
2 = 20 -30	0.417902	0.83	0.346858
3 = 30 -40	0.512632	0.80	0.410106
4 = 40 - 50	0.545532	0.75	0.409149
5 = 50 -60	0.512632	0.67	0.343464
6 = 60 -70	0.417902	0.56	0.234025
7 = 70 - 80	0.272766	0.40	0.109106
8 = 80 - 90	0.0947305	0.25	0.0236826
Sum	3.14159		2.18971

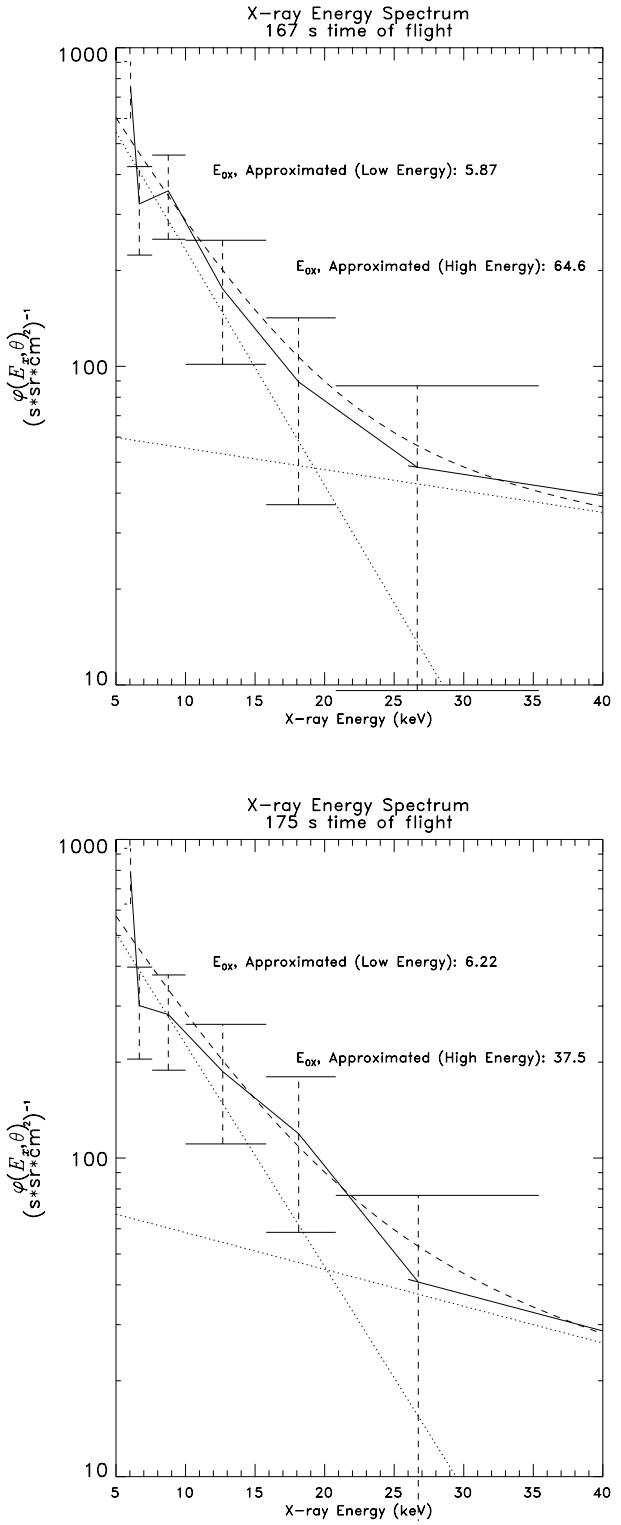

Figure 15. X-ray energy spectra for 167- and 175-s flight time, in lin-log scale. *Solid line*: measurements in azimuth sector 0˚ to 30˚, with error bars (statistical fluctuations) indicated. The channels 10.0-12.3 keV and 12.3-15.8 keV are added. *Dotted line*: two exponential approximations. *Dashed line*: the two exponential approximations added.

the same spectra as shown in the two upper panels of Figure 10 on page 38, Paper 1). We have also replotted the upper panel of Figure 11 on page 39, Paper 1, which is shown in Figure 16. The average discrepancy between directly measured electrons and derived electrons from X rays, integrated in the energy range from 10.8 keV to 250 keV, is now 4% (instead of 27% [Paper 1]) but the correlation has decreased from 0.6 to 0.52. However, these improved results are just minor adjustments having no influence on the conclusions in the paper.

The good results reported in this study [Paper 1] were provided by the combined use of the results from different studies that constitutes a complete method to derive equivalent isotropic fluxes and spectra of electrons from the angular-dependent precipitating electrons and from the angular-dependent X-ray measurements.

1. When deducing the electron spectra from the X-ray spectra, we used a sum of two exponentials to represent the measured X rays. This was found to represent the X-ray spectrum quite properly and has also been reported from other rocket X-ray measurements during the early recovery phase [Goldberg et al., 1982].

2. We transposed the anisotropic fluxes to equivalent isotropic fluxes of electron precipitation, using results from Mæhlum and Stadsnes [1967], as the models [Seltzer and Berger, 1974; Walt et al., 1979] assume isotropic fluxes of the electrons.

3. By combining the two models [Seltzer and Berger, 1974; Walt et al., 1979] we were able to take into account that the X rays are not emitted isotropically from the production layer. The preference for near horizontal escape angles is significant for all energies and most pronounced at the higher X-ray energies.

Following this procedure we obtained a combined model for deducing electrons from X rays. The discrepancies in our calculations were well within the errors due to uncertainties, resulting from the instruments and the geometry of the observations. Although our results showed satisfactory agreement between observed and derived electron fluxes and spectra, there are still shortcomings in the inversion technique used in this study.

1. In the paper of Walt et al. [1979] the angular distribution of X rays propagating out of the atmosphere is given only for five different e-folding energies of the electron spectra. In the inversion process one thus have to interpolate between these distributions and this introduces some uncertainty. As described in Section 2.3 the code developed from Lorence [1992] enables us to calculate the X-ray angular distribution in zenith angular intervals of ~10˚, providing a significant improvement of the inversion technique, which were used for the PIXIE data and will be discussed in Section 5.4

2. The theoretical models by Seltzer and Berger [1974] and Walt et al. [1979] assume an exponential shape of the electron energy spectrum. This is clearly an idealization of the real shape of the electron energy spectrum which sometimes may be fairly good but in other cases not so good at all. Both Maxwellians and exponentials have been widely used to represent the electron spectrum, but as only electrons >5.6 keV in this study (and >3 keV in the PIXIE measurements) produce measurable X rays, these two distribution functions are very similar, regarding X-ray production at energies above the low-energy threshold of our instruments. By using the double exponential representation we were able to take into account the frequently observed hard tail in the electron spectrum. However, others [e.g., Christon et al., 1991; Sharber et al., 1998] have found that a Kappa function is even better to represent the hard tail of the electron spectrum. This will be discussed later in connection with the PIXIE studies, see Section 5.4.

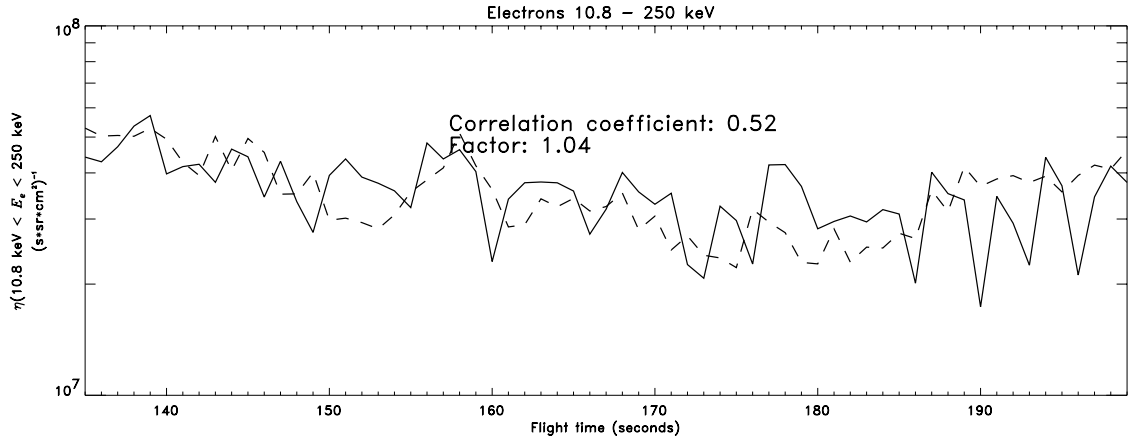

Figure 16. Calculated electrons from differential X-ray spectra and directly measured electrons, equivalent isotropic integral fluxes. *Solid Line*: Electrons integrated from 10.8 keV to 250 keV, calculated from X-ray differential spectra (5.6 - 100 keV) measured in the azimuth sector from 0˚ to 30˚. *Dashed Line*: Directly measured electrons, integrated from 10.8 keV to 250 keV.

3. Seltzer and Berger [1974] and Walt et al. [1979] assumed isotropic fluxes of precipitating electrons. In our case we observed an anisotropic electron precipitation. In our calculations of the equivalent isotropic electron distribution, we have assumed that the X-ray production from monoenergetic electrons is proportional to the number of electrons absorbed in the atmosphere. We do not know how good this assumption is.

4. Both Seltzer and Berger [1974] and Walt et al. [1979] assumed homogeneous electron precipitation over wide horizontal areas. This is most often not the case in reality and it is clear that the geometry of the electron precipitation regions will influence the angular distribution of the X rays leaving the atmosphere. Assuming uniform precipitation, the van Rhijn effect will influence the calculation of the angular distribution of X rays to a large extent. In the case studied in Paper 1 we observed both arc fragments and patches, and as the detector was looking at slant angles at the source region the van Rhijn effect will be different from the uniform precipitation case, causing some uncertainty in the calculations.

From the study presented in Paper 1 we may conclude that using proper inversion procedures, X-ray measurements was proven to be a powerful technique to derive the spatial, temporal and energy distribution of the energetic electron precipitation.

5. Global X-ray imaging by PIXIE

With the PIXIE instrument on board the Polar satellite a new era of X-ray measurements was initiated. The global images taken during apogee passes enable us for the first time to study the dynamics of the entire global X-ray aurora. In this section we will briefly describe some of the problems we encountered in the image processing and how we solved them. We will also discuss the main results from our analysis of the PIXIE data, which are reported in 2 published papers [Paper 2; Paper 3] and 2 submitted papers [Østgaard et al., 1999d, hereafter called Paper 4; Paper 5].

5.1. The PIXIE instrument and image processing

For a detailed description of the image processing procedure we refer to Technical Report and here we just want to point out some main aspects of the image processing.

PIXIE is a pinhole camera with four stacked multiwire proportional counters as detecting elements. Two detectors are in the front chamber, which contains a 1.1 atm Ar/CO_2 mixture, has a 0.1 mm Be entrance window, and is sensitive to X-ray photons from ~2 to ~10 keV. The rear chamber, with a 2 atm Xe/CO_2 mixture and a 2 mm Be window, contains the other 2 detectors and covers the energy range from ~10 keV to ~60 keV. Generally the photons are stopped by photoelectric absorption in the detector gas. The photon energies are revealed by the amplitudes of the anode signals and are digitized into 64 energy channels for each layer. The corresponding induced signals in the surrounding cathode wires provide the X and Y positions of the interaction and is read out through a graded density wire structure [Gilvin et al., 1981]. Thus every X-ray photon is recorded separately with energy, position and time. The graded density position read-out system has some inherent non linearities. To correct for these a look-up table was included in the instrument electronics in order to linearize the position coordinates.

As for all space borne instruments properly calibration was provided before launch both regarding spatial determination and energy response. Correction of the count rates due to dead time in the instrument, the read out system and the telemetry were all well known and rather straight forward to correct for. What causes the main problem for the PIXIE instrument was the change of temperature relative to the expected operational temperature. The instrument was calibrated for operating at slightly below room temperature, as predicted by the pre-launch thermal simulation, but soon after launch it became obvious that the temperature was usually below -10˚C. This large change, i.e., ~25˚, introduced unknown gain shifts and signal offsets in the instrument electronics, which made the pre-launch calibrations, both the spatial determination and the energy response, almost useless. Thus a complex correction scheme had to be established in order to correct for these errors.

The main effects of the unknown gain shifts and signal offsets are:

1. The position coordinate linearization by the look-up table works more like a 'scrambler' rather than a correction procedure. The position corrections routines now have to be energy and temperature dependent and each wire layer (cathode) now behaves differently.

2. The instrument energy calibrations taken at near room temperatures are no longer valid.

Additional problems which appeared during flight:

3. The front chamber (the low energy section of the instrument) developed an intermittent high voltage supply problem, which is resolved by duty cycling the high voltage supply. In the early stage this instrument section could be operated at less than 10% duty cycle, but later one has obtained up to 80% duty cycle, which is quite satisfactory.

4. A gradual increase of the gain in the front chamber which is interrupted by a smaller decrease during each biannual flip of the satellite.

Since PIXIE analogue electronics temperatures spend most of its time below -10˚C we have concentrated on developing a correction procedure for this temperature range, and we are at present able to provide X-ray images and X-ray spectra with a spatial resolution only dependent on the geometry of the camera and statistical error due to the count rates of the auroral X rays. Basically there were three different kind of correction schemes to be made. 1. Background subtraction. 2. The position determination. 3. Energy calibration.

5.1.5. Background Subtraction. For a time interval to be classified as background interval we required:

1. Analogue electronic temperature is below -10˚ C.
2. No auroral X rays nor celestial X rays are visible.
3. Satellite at radial distances greater than 6 R_E.

As the position determination due to the signal offset were both time and energy dependent we have sampled background matrices for different periods of time and for 5 different energy bands in each layer. The separation in 5 energy bands was chosen in order to improve the statistics in each energy band. As we found that the fluorescence peak and the background noise to dominate the count rates in anode 3 above channel 22, we have sampled the background for this anode in two energy bands, channels 10 through 15 and channels 16 through 21. These background matrices are now used for subtraction.

As background radiation we consider all radiation which are not X rays produced by precipitating electrons in the atmosphere. There are at least 3 sources for this background radiation.

1. X-ray bremsstrahlung produced when energetic electrons strike the structures surrounding the chambers. These X-ray photons will probably enter the detector chambers almost isotropically, with some preferences of radiation from the sides and the rear due to the location of the surrounding structures.

2. Cosmic X rays coming in through the pinholes. These X rays will be detected during apogee passes when the Earth does not cover the whole field of view of PIXIE.

3. Minimum ionizing particles passing through the chambers and avoiding the veto system.

Compared to the contribution from minimum ionizing particles we found the X ray background to be dominant. This means that in addition to be used for background subtraction the information of non-linear effects in the background can be used to correct for the non-linear effects seen in the auroral X-ray images for both the front chamber and the rear chamber. Thus an algorithm to redistribute the auroral X-ray counts were established [see Section 5.2, Technical Report].

5.1.6. The Position Determination. After applying the non-linearity correction procedure (Figure 10 on page 103, Technical Report) there are still two more steps in order to establish the correct coordinates for the images. First, applying large-scale factors provides that the distance between the sub-images is consistent with the distance between the pinholes. Finally the center of the focal plane has to be determined for all the layers. The position of the neutron-star binary Circinus X-1 X-ray source is accurately known. By comparing the nominal and observed locations of its image an absolute position calibration is obtained for center pixels of the first two detector layers. Due to the softness of the spectrum from Circinus X-1 the method can only be applied to the front chamber. To determine the center pixel in layer 3, i.e., determining the true mechanical position of the layer 3 pixels, we used X-ray events with bright narrow spots visible in both layers and shifted the layer 3 image around until we obtained the best spatial correlation with layer 1.

5.1.7. Energy Calibration. Energy calibration is performed by two internal X-ray calibration sources, one at 5.895 keV for anodes 1 and 2, and another at 22.1 keV for anodes 3 and 4.

As discussed in Section 2.3 the line emission from Ar must be taken into account when the detector uses Ar as stopping gas. For PIXIE the Ar line has been successfully utilized during calibration run as the Ar escape peak is seen at 2.9 keV, i.e., 5.895 keV - 2.96 keV (where 2.96 keV is the Ar K-α line) providing two calibration points and thus enabling determination of both the gain and offset for this layer. When detecting auroral X rays the Ar escape peak will be distributed through the entire energy range, i.e., at E_X - 2.9 keV with an intensity less than 7-8% of the incoming X-ray photon with energy, E_X, and the error from this effect is therefore negligible. The energy calibrations have revealed an unexpected gain drift in the front chamber, which is seen as a gradual displacement of the calibration peak towards higher channels interrupted by a smaller decrease during each biannual flip of the satellite. Examination of these temporal changes resulted in a linear relation between the calibration peak (P_C) and the day number (d_N), as given by (14) (A and B are constants).

$$P_C = A \cdot d_N + B \tag{14}$$

This relation is documented in Figure 6 on page 100, Technical Report. Furthermore, based on the two peaks from the calibration run the relation between offset and calibration peak was also found to be linear. Given the temporal changes of both the gain and offset the energy of each X-ray photon in the front chamber can be properly determined.

For the rear chamber, filled with Xenon gas, we obtained only one peak from the calibration run, i.e., at 22.1 keV (or a double peak, see Figure 5 on page 100, Technical Report). To obtain an estimate of the offset in the rear chamber we based our reasoning on the fact that in general an X-ray bremsstrahlung spectrum has to be monotonously decreasing towards higher energies. Furthermore, an eventual hinging point (i.e., the transition from one dominating e-folding energy to another) shall not necessarily be at the intersection of the ranges of anode 1 and anode 3. By applying a non-zero offset to the energy spectrum of anode 3 we found it possible to a large extent to comply with these constraints, as shown in Figure 7 on page 101, Technical Report.

5.1.8. Time and Spatial Resolution. The spatial resolution is determined by the pinhole size and corresponds to ~1000 km and ~150 km in the X-ray source region in the atmosphere, for apogee and perigee passes, respectively.

The time resolution for the global auroral images are deter-

mined by the counting statistics and is therefore better for the lower than for the higher energies, due to the shape of the X-ray bremsstrahlung spectrum. For apogee passes we have found that 5 min accumulation time is a proper choice for the rear chamber, but down to 1-2 min can be used for the front chamber. For the perigee passes these accumulation times can be lowered considerably, due to the much higher counts rates, but so far we have not systematically studied any events during perigee passes. The accumulation times given here are for moderate events and can be lowered for stronger events. To study temporal changes during the apogee passes at even better time resolution, we have integrated properly defined areas giving a time resolution down to ~30 s, which is comparable to imaging techniques at other wavelengths. As we record every X-ray photon separately with energy, position and time, the time resolution can be adjusted according to the strength of the event. Compared to previous X-ray imaging instruments the PIXIE camera represent a huge improvement regarding the global coverage and time resolution. However to study fine spatial features, X-ray instruments onboard low-altitude satellites are more suitable, e.g., the UARS PEM/AXIS.

By isolating the different processes taking place in the PIXIE camera and providing calibration and correction in a modular step procedure we believe that the spatial resolution for the processed PIXIE image is now restricted basically by the geometry in the camera and the statistically errors due the low count rates of X-ray bremsstrahlung from the ionosphere. We also think the way we have proceeded give us the X-ray energy spectra in 6 energy bands (4 from the front chamber and 2 from the rear chamber).

5.2. Global dynamics of substorms observed in X rays and UV

Motivated by the electron precipitation morphology found in the statistic studies of cosmic radio noise absorption [Berkey et al., 1974], in-situ particle measurements [McDiarmid et al., 1975; Hardy et al., 1985] and X-ray measurements from balloon campaigns [Sletten et al., 1971; Kangas et al., 1975] we initiated a statistical study of the development of isolated substorms by comparing global images at two different wavelengths, i.e., UV and X rays from the two cameras onboard Polar (UVI and PIXIE). The study is presented in Paper 2 and here we will briefly discuss the main results of the paper.

Due to the low duty cycle of the front chamber in the early stage of the mission only the rear chamber of the PIXIE instrument could be used to study the continuous time development of substorms during 1996. Here it should be mentioned that without the effort from the Bergen PIXIE group to develop the image processing scheme from both the front and rear chamber as described in Technical Report this study could not have been accomplished. While the UVI LBHL band, used in Paper 2, responds to the total electron energy flux, which is usually dominated by electron energies <10 keV (see Section 2.2), the PIXIE X-ray images from the rear chamber are in the energy range of 9.9-19.7 keV, which are X rays produced by electron energies >~10 keV. Thus, for this study the UVI and PIXIE provide images from complementary ranges of electron energies, well suited to examine differences in the low- and high-energy range of electron precipitation. With this ability to follow both the spatial and the temporal development of substorms in a wide energy range we were able to verify the results and the suggestions put forward in the papers mentioned above and establish a more comprehensive picture of the energetic substorm.

We looked through the entire data set of PIXIE measurements from 1996. As mentioned in Section 5.1 our image processing scheme was only valid during times of low temperature of the analogue electronics (<-10˚C) and thus only measurements from late May to early Oct. and from late Nov. and throughout Dec. (see Figure 2 on page 98, Technical Report) could be used for this study. To be included as isolated substorms for this study we also demanded that:

1. The provisional AE index from Kyoto data set showed significant signatures of isolated substorms.

2. During apogee passes UVI and PIXIE both covered the substorm onset and the main part of the recovery phase.

We found 14 isolated substorms during 1996 which complied with these constraints [Paper 2]. Later we included 2 events from 1997 when both the front chamber and rear chamber were operating (presented in Paper 4). For each of these substorms we examined energetic particle measurements from geosynchronous altitude from a set of satellites operated by Los Alamos National Laboratory (LANL) and the NOAA Geostationary Operational Environmental Satellite (GOES). Measurements from all these satellites were used in this study depending on their locations for the different events. As the X-ray emission observed by the PIXIE rear chamber is primarily generated by electrons with energies 10-100 keV, we mainly focused on the lower-energy channels (50-500 keV) when we compare the ionospheric X-ray fluxes to electron injections seen by the LANL satellites. For comparison between PIXIE and GOES the lowest electron integral channel (>600 keV) is used. As we often observe injections of both electrons and protons during the substorm onset, we also inspected the injection signatures seen in the proton measurements from the LANL and the GOES spacecrafts. Solar wind data from the Wind satellite and ground-based magnetic measurements from International Monitor for Auroral Geomagnetic Effects (IMAGE), Canadian Auroral Network for the OPEN Program Unified Study (CANOPUS), or Sodankylä have also been studied for each event. The CANOPUS and IMAGE networks were used for comparison when the onset took place during 02-10 UT and 13-18 UT, respectively. The results are listed in Table 1 on page 51, Paper 2.

When displaying the substorm development as seen in UV and X rays one significant difference appeared to be very obvious for almost every substorm. Delayed relative to substorm onset a maximum of X-ray emission appeared around 5-9 MLT, which were rarely seen in the UV images. To study this feature and especially the time delays between the substorm onset and the onset of the morning maximum of X-ray emission, we wanted to examine the time development of the X-ray substorm along the auroral zone at the finest time resolution. By using 5 min accumulations of the global X rays sampled every 30 s, integrating separately in every 2 hour MLT sector between 60˚ and 74˚ CGM latitude we obtained a time resolution of about 1 min. The end of the accumulation time interval was used for the timing of onset. To improve the statistics 2 hour MLT sectors were chosen. For fluxes of 250 $(\text{keV s sr cm}^2)^{-1}$ the σ is ~20%, and for 100 $(\text{keV s sr cm}^2)^{-1}$ the σ is ~30%. The result of this procedure is shown in e.g., Figure 3 on page 49, Paper 2.

Paper 2 represents the first study ever of the global features of the energetic precipitation compared to the softer part of the precipitation using remote sensing techniques at two different wavelengths, i.e., UV and X rays. The main results were as follows.

1. Growth phase signatures of directly driven precipitation at dawn and dusk were not seen by PIXIE but were common features in the UV substorms, indicating mainly soft precipitation. Growth phase signatures as those reported by Pytte and Trefall [1972] were not observed. This may be attributed to the higher sensitivity

of the scintillator and Geiger-Müller tubes used for the balloon campaigns. A study focusing on substorm onsets when both the front and rear chambers of PIXIE are operating will probably reveal more information about this. Such a study has been initiated by the Bergen group and some preliminary results were reported by Stadsnes et al. [1998].

2. The substorm onsets were seen simultaneously by UVI and PIXIE and correlate very well with both the injection signatures seen at geosynchronous orbit and the ground-based magnetic measurements (see Table 1 on page 51, Paper 2).

3. During the expansion phase the most intense UV emissions were observed at duskward part of the bulge, while the most intense X rays were moving dawnward. Thus the westward movement or the WTS, which is believed to be a common feature during the expansion phase of the substorm [Akasofu, 1964; Meng et al., 1978] is not a common feature when looking at the energetic electron precipitation during the expansion phase. Only occasionally did we observe a significant westward movement of X-ray features, similar to what Berkey et al. [1974] have reported, and we may conclude that the WTS is basically a low-energy phenomena (<10keV) which only occasionally include energetic electron precipitation (>10 keV). An example of the latter is shown in Figure 17, i.e., a westward expansion from substorms onset in the 20-22 MLT sector into the 19-21 MLT and 18-20 MLT sectors.

4. During the recovery phase a maximum of X-ray emission was seen in the morning sector, which confirms the results found by others [Jelly and Brice, 1967; Berkey et al., 1974; McDiarmid et al., 1975; Hardy et al., 1985]. In both the UV and the X-ray substorm we saw eastward motion of the precipitation area, but the maximum in the morning sector is a common feature only in the X-ray substorm. As 3 of the substorms in our data set happened to have substorm onset in the same local time sector we normalized and superimposed these substorms in order to represent an 'average' X-ray substorm, as shown in Plate 2 on page 52, Paper 2. Compared to the schematics proposed by Akasofu [1968] the main difference is that the morning maximum is very significant in our 'average' X-ray substorm.

5. On the basis of the time development of X-ray fluxes in 2 hour local time sectors we determined the time and location both for the substorm onset and the first enhanced X-ray fluxes seen in the morning sector, which can be related to the injection in the midnight sector. By using drift models of the gradient and curvature drift of electrons [Lew, 1961, Roederer, 1970], we found the time delays of 9 substorms from 1996 to be consistent with drifting electrons in the energy range of 90-120 keV (Figure 7 on page 53, Paper 2). In a review [Paper 4] of this result we plotted only the time delays where both the substorm onset and the onset in the morning sector were well-defined (i.e., the first category of 1996 substorms) and added 2 more substorms from 1997 and found the time delays to be consistent with drifting electrons in the energy range of 90-170 keV (see Figure 5 on page 75, Paper 4). On the basis of these results we conclude that the maximum of precipitation observed in the morning sector is not caused by any new source region in the magnetosphere but rather to electrons injected close to midnight, drifting into the morning sector because of their gradient and curvature drift in the inhomogeneous magnetic field.

Based on our findings in this study we also suggested 2 possible candidates of explanations for the observed morning maximum.

1. One candidate for such a mechanism is the wave-particle interaction between VLF waves and electrons, i.e., the doppler-shifted cyclotron resonance of anisotropic electron fluxes and whistler mode waves.

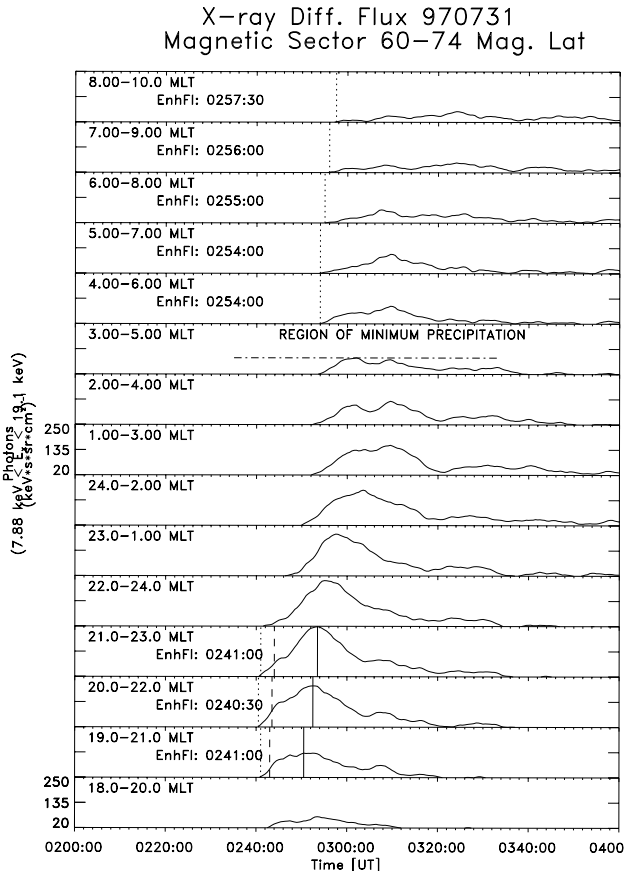

Figure 17. Time development of the mean differential X-ray fluxes in sectors from 18-20 to 8-10 MLT and fixed magnetic latitude 60˚-74˚. Dotted lines indicate the first enhancement of the mean differential X-ray flux, the dashed line indicates the sectors with the largest increase rate of fluxes and solid lines are the first maxima.

2. Another candidate is more straightforward. Equatorial mirroring energetic electrons injected in the midnight sector from the inner edge of the plasma sheet (5-7 R_E) will drift along contours of constant magnetic field strength when the influence of the convective electric field can be neglected (i.e., for electrons >~100 keV). These contours are fairly asymmetric [Fairfield, 1968] and will cause the electrons to move outward as they drift into the morning sector. During disturbed conditions the magnetosphere is compressed, and the dawn magnetopause could well be at 11-13 R_E. Such values are obtained when the solar wind measurements are used to estimate the dawn magnetopause position. We did this for 9 of the substorms presented in Paper 2, when the morning maximum could be well identified. The estimates of the dawn magnetopause location are based on evaluating the stand-off distances, R_{ST} given by (15) [Walker and Russell, 1995],

$$R_{ST} = 107.4(n_{sw}u_{sw}^2)^{-\frac{1}{6}} \quad (15)$$

where n_{SW} is the solar wind density and u_{SW} is the solar wind bulk

speed and the relation between the locations of the subsolar and the dawn magnetopause found by Sibeck et al. [1991]. Based on measurements from ~1000 magnetopause satellite passes for a large range of solar wind pressure conditions Sibeck et al. [1991] found the relation between solar wind pressure and subsolar magnetopause location as shown by solid line in Figure 18a. The triangles and crosses show the R_{ST} positions for the 9 substorms calculated from (15) with the measurements from the Wind satellite as input. In Figure 18b the solid line shows the relation between the locations of the subsolar magnetopause and the dawnside magnetopause as found by Sibeck et al. [1991] and the triangles and crosses show the dawnside magnetopause location for the 9 substorms using the same relation as Sibeck et al. [1991] found. It is seen that dawnside magnetopause location at 11-13 R_E correspond to the high solar wind pressure events. If this is the case the energetic electrons may drift into the magnetopause. In this region the conservation of the 1. adiabatic invariant breaks down, and the electrons will be scattered into a fully isotropic distribution. For the events where the peak intensity of X-ray emission was found at 66˚-67˚ CGM latitude this explanation is probably not appropriate. However, for the other half, where the peak intensity was found at 70˚-71˚ CGM latitude, the source region may be identified closer toward the magnetopause [Newell and Meng, 1994] as discussed in Section 4, Paper 2. Disregarding for the moment that field lines are stretched towards the tail in the flanks we assume that the magnetic field is approximately dipole shaped in the dawn region, as extracted from the data set from Isenberg et al. [1982] (see Figure 19 on page 24). Thus we can use the simple relation given by

$$L = \frac{1}{(\cos\lambda)^2} \tag{16}$$

which traces the magnetic field line at L=11-13 in the equatorial plane down to λ=72.4˚-73.8˚ magnetic latitude, which is only 1.5˚ poleward of where we observe the X-ray emission for half of the events.

These candidates of explanations will both be discussed further in Section 5.5 when both X-ray features and in-situ electron measurements from passes through the region of the morning precipitation are examined [Paper 5].

5.3. A study of substorm onset triggering processes, PIXIE and Geotail

One of the events used in the statistical study, i.e., the substorm event on December 10, 1996, happened to occur during a time period when Geotail was very well located in the distant tail [-25, 2, -2] R_E in geocentric solar magnetospheric (GSM) coordinates, in order to observe the substorm evolvement and the occurrence of reconnection processes. The study which is presented in Paper 3 was based on a large data set from many spacecrafts and ground based measurements and extensively utilized the opportunities given by the International Solar Terrestrial Physics (ISTP) program. The primary data basis for this study was the High Energy Particle - Low energy particle Detector experiment (HEP-LD) on board the Geotail spacecraft, run in a special plasmoid mode and the PIXIE X-ray camera. In addition, magnetic measurements from Geotail, UV images from Polar, ground-based magnetic measurements from high-latitude and mid-latitude stations and particle measurements at geosynchronous orbits (LANL) as well as solar wind measurements by the Wind satellite were examined. The aim of the study was to study the substorm event in the context of substorm triggering processes and theories proposed to explain substorm growth phase and expansion phase. We also performed mapping of the X-ray intensity contours along the field lines into the equatorial plane of the CPS, using a model by Tsyganenko [1995] in order to identify the source regions of the energetic precipitation (see Plate 2 on page 63, Paper 3). The mapping results were found to be consistent with the in-situ particle measurements of injection signatures in the tail (Geotail) and at geosynchronous orbit (LANL).

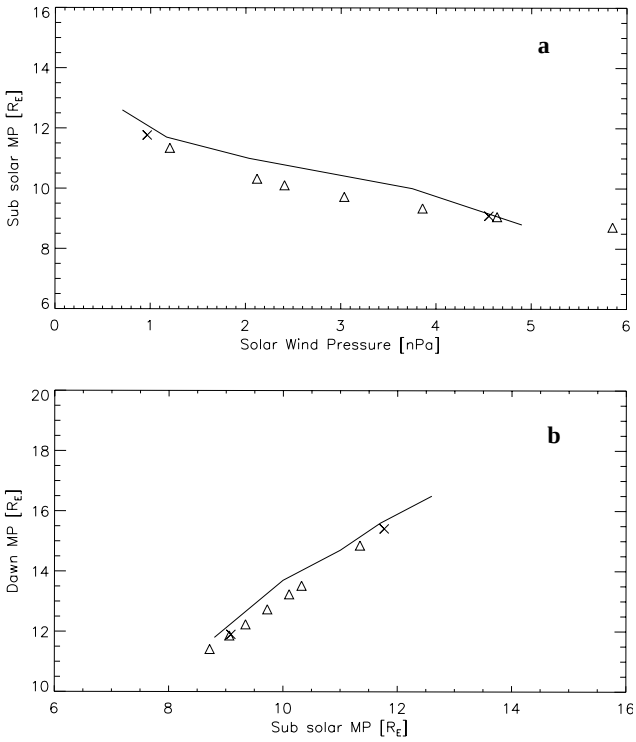

Figure 18. Estimates of the location of the dawnside magnetopause for 9 of the substorm events in our data set. (a) Location of the subsolar magnetopause as a function of solar wind pressure. Solid line is the measurements from Sibeck et al. [1991] and triangles and crosses are from our data set using the R_{ST} distance as the subsolar magnetopause location (15). (b) Location of the dawnside magnetopause as a function of the subsolar magnetopause location. Solid line is the measurements from Sibeck et al. [1991] and triangle and crosses are from our data set when using the relations for different solar wind pressure conditions given by Sibeck et al. [1991].

During the substorm event, which was associated with a weak magnetic storm that started the day before, two onsets could be identified; 1704 UT and 1736 UT. In addition, there was a transient energetic precipitation event at 1720 UT. The first onset involved predominantly low energy electrons, as this was only seen in UVI LBHL band emission (i.e., electron energies <10 keV) while the second also included the energetic electrons, measured by PIXIE rear chamber (electron energies >10keV).

Prior to the substorm onset at 1704 UT the magnetic measurements from Geotail indicated a stretched tail configuration, and although the B_Z component of the interplanetary magnetic field (IMF) was close to zero the energy input to the magnetosphere was above the substorm level (>10^{11} W) [Akasofu, 1981], primarily due to the large solar wind velocity observed by the Wind sat-

ellite at that time (see lower panel of Figure 2 on page 59, Paper 3). To estimate the energy input to the magnetosphere at the subsolar magnetopause the classical Akasofu ε parameter [Perrault and Akasofu, 1978] was used

$$\varepsilon = vB^2\left(\sin\frac{\theta}{2}\right)^4 l_0{}^2 (\mathrm{ergs}\cdot\mathrm{s}^{-1}) \qquad (17)$$

where v is the bulk speed of the solar wind, B is the strength of the IMF, θ is the clock angle of the IMF, i.e., $\theta = \tan^{-1}(|B_Y| / |B_Z|)$ for $B_Z > 0$ and $\theta = 180^\circ - \tan^{-1}(|B_Y| / |B_Z|)$ for $B_Z < 0$ and l_0 is an empirically determined scale length for the interaction to occur and is usually set to 7 R_E.

5.3.1. Growth Phase Signatures. At 1654 UT a small flux rope is launched as a result of enhanced reconnection earthward of Geotail (see B_Z and B_Y in Plate 1 on page 60, Paper 3), but no other measurements indicate any breakup signature. UV images show a typical growth phase brightening which may be interpreted as a response to the reconnection event combined with the existing weak precipitation related to a stretching of the tail and subsequent particle scattering at the earthward boundary of the plasma sheet [Sergeev et al., 1983]

5.3.2. Expansion Phase and First Onset. The first onset was identified at 1704 UT from the pulsation measurements at Sodankylä (Figure 3e on page 61, Paper 3). At the same time a larger flux rope passes above Geotail and the UV images (Plate 3f and 3g on page 65, Paper 3) show an azimuthally and northward expanding bulge. No energetic precipitation is seen in the X-ray measurements indicating mainly soft precipitation. This was also supported by plasma data from Geotail. This onset may be related to the northward turning IMF B_Z observed at 1648 UT at the Wind satellite (Figure 2 on page 59, Paper 3). The time delay of 16 minutes is in agreement with the expected time delay of 10 - 16 minutes, using methods described by Sergeev et al. [1986] and Kan et al. [1991].

At 1720 UT a transient energetic precipitation event is seen in the X-ray images, emerging at the poleward edge of the existing UV bulge. The mapping result of the X-ray emission contour indicates a source region for this precipitation to be tailward of Geotail. In the UV images, which primarily reflect the soft precipitation, a quite different development of the substorm is seen at this time. Here, the existing bulge continues to expand northward and azimuthally. Consistently with the expansion of the UV features the downward field aligned currents (FACs), inferred from magnetic measurements at mid-latitudes [Sergeev et al., 1996], move eastward, while the upward FAC moves westward, as shown in Figure 5 on page 62, Paper 3.

The early stage of the expansion phase of this substorm emphasizes very clearly how differently the substorm characteristics are observed depending on the energy range we examine. The soft precipitation seen in the global UV images displays an entire substorm development, while the energetic precipitation depicted by PIXIE only shows a transient and spatially limited event occurring at 1720 UT. The source region for the soft precipitation observed in the UV images is clearly earthward of Geotail - probably close to the inner edge of the plasma sheet, whereas the energetic precipitation maps to a source area tailward of Geotail (Plate 2 on page 63, Paper 3). The substorm is neither very intense nor very explosive, and there are no distinct injections at geosynchronous orbit. The low energy input from the solar wind prior to this onset can account for the weak and slow nature of this onset.

The persisting precipitation area observed in the UV images expands poleward, enhancing at the same time and at the same location as the transient energetic precipitation occurs. The precipitation in the entire region will account for a build up of conductivity in the ionosphere at different altitudes according to the energy differences. Such a preconditioning helps the ionosphere to support and close the field aligned currents resulting from the current diversion in the magnetosphere.

5.3.3. The Second Onset. The global PIXIE (and UV) images demonstrate that the breakup at 1736 UT, which includes energetic injection and precipitation, takes place on the equatorward western edge of the existing precipitation area. Although magnetic field line mapping during such disturbed conditions is subject to large uncertainties, the source area of the auroral breakup locates to a position well earthward of Geotail, possibly close to geosynchronous orbit (Plate 2 on page 64, Paper 3). The ground magnetic response to the breakup shows significant Pi2 pulsations and the magnetic measurements at mid-latitudes indicate intensification of both the downward and the upward FAC - the latter moving rapidly duskward.

Due to a large negative IMF B_Z prior to this onset a large amount of energy has been transferred into the magnetosphere for ~20 minutes prior to this onset. The higher energy input may account for the stronger and more explosive nature of this onset compared to the first onset.

The current wedge derived from ground magnetic measurements correlates very well with the features of soft precipitation, while the energetic precipitation seem to correlate very well with the injection signatures from Geotail and LANL.

Although the revised NENL models [e.g., Shiokawa et al., 1998] does not rely on any external trigger mechanism, we note that the IMF B_Z turns rapidly northward around 1723 UT. The time delay of 13 minutes is in good agreement with the expected propagation times of solar wind discontinuities.

5.3.4. Mechanism for Substorm Onset. The observations from Geotail are consistent with the interpretation that the substorm activity is associated with magnetic reconnection in the midtail plasma sheet (~ 25 R_E) prior to both onsets. However, the PIXIE and UV images combined with the mapping results locate the source regions for the breakups to the near-Earth region. The interpretation of the substorm development is illustrated in Figure 6 on page 67, Paper 3.

One model which is consistent with the observations for this particular event is as following; magnetic reconnection occurs sporadically in the extremely thin plasma sheet in the near-Earth tail and midtail throughout the growth phase. Consequently, plasma will be accelerated both in the earthward and tailward direction at the reconnection site. The fact that the field lines on the earthward side connect to the Earth produces an important asymmetry. Unless rapid transport- or loss mechanisms operate, plasma ejected earthward will accumulate and the density and pressure gradients will build up. In the unstable conditions caused by these parameters, there may be a number of candidates responsible for the current disruption and explosive onset of substorms. For the particular substorm event studied here, changes of the solar wind IMF seems to trigger the breakups.

5.3.5. Conclusion.

Our main conclusions in Paper 3 are as follows:

1. Signatures of magnetic reconnection are observed in the midtail region prior to both onsets. The reconnection occurs sporadically and burst like.

2. Both onsets are manifested by electron precipitation at global scale, field aligned currents and Pi2 pulsations.

3. The solar wind input energy prior to the first onset was low compared to the second onset.

4. The source region of the energetic precipitation during the first onset is tailward of Geotail while the corresponding source region for the soft precipitation is well earthward of Geotail.

5. The second onset includes both soft and energetic electrons. The difference in solar wind input energy prior to the two events can probably account for the different nature of the two onsets.

6. Both onsets appear to be triggered externally by the northward turning of the IMF B_Z.

7. The source region expands both azimuthally and radially. The expansion is reflected in the precipitation area and ground magnetic perturbations.

8. The study presented here provides support to many of the key elements of the revised NENL model; Reconnection around 25 R_E generates fast earthward plasma flow which is detected by Geotail. We do not have any direct observations of the flow braking and diversion process thought to take place at the boundary between dipolar-like and tail-like magnetic field. In the revised NENL model, the FACs are assumed to be a result of this braking process. The observed Pi2 pulsations may be a consequence of compressional pulses as postulated by the NENL model, although we do not have any observations to confirm this.

9. The NENL model can not account for all of the observations during the substorm event studied. The explosive nature of the onset and the close relation between the onsets and solar wind changes indicates that some kind of triggering mechanism is involved. Furthermore, individual features like e.g. the transient precipitation event seen during this particular substorm does not easily fit into any standard model.

5.4. Derivation of electron spectra from X rays spectra

Motivated by our findings in the statistical study of global X-ray features [Paper 2] we wanted to study the frequently observed morning maximum of X-ray emission in the morning sector in more detail. To do this we search for isolated substorms during 1997, following the same selection criteria as for the statistical study but also demanding that both the front chamber and the rear chamber of the PIXIE instrument were operating, in order to provide spectral information about the X-ray emission in the morning sector. We also found it necessary to develop a method for deriving the electron spectra from the X-ray spectra from PIXIE and compare these spectra with directly measured electron spectra from low-altitude satellites. We found two isolated substorms which complied with our constraints, July 31 and September 4. In Paper 4 the first results from the comparison of low-altitude passes by DMSP and NOAA-12 through the region of morning precipitation are shown and in Paper 5 both the comparison of measured and derived electron precipitation profiles and spectral characteristics are shown.

To examine the properness of our inversion technique from X rays to electrons we wanted to do the comparison both ways, by comparing calculated X-ray production from measured electrons with directly measured X rays and by comparing derived electron precipitation from the X-ray measurements with directly measured electrons. For both these comparison we used the tables provided by a code developed from the transport code by Lorence [1992]. These tables are calculated for exponential electron spectra and yield the angular X-ray production in the upward hemisphere (see Section 2.3). As the angular X-ray production is given in ~10˚ intervals we were able to take into account the effect of PIXIE viewing the ionosphere at slant angles.

To calculate the X-ray production from the electron measurements from DMSP and NOAA-12 satellites we found that electron spectra both at midnight and in the morning sector can well be represented by double (or single) exponentials. It should be noted that a Kappa function would probably have been more suitable to represent the hard tail of the morning side spectrum, as proposed by others [e.g., Sharber et al., 1998], but as our X-ray calculation procedure only allows exponentials and Maxwellians, we used double exponential fits keeping in mind that the electron fluxes might have been slightly underestimated for the high energies. For the NOAA-12 passes we also compared the directly measured energy flux with the energy flux we obtained from the double exponential fit to the measurements from the two detectors. The agreement was found to be acceptable as shown in Figure 4 on page 85, Paper 5.

Based on the assumption of the double exponential representation of the electron spectra we calculated the X-ray production along the satellites trajectory and compared with the directly measured X rays from PIXIE. The measured X rays along the magnetic footprint of the satellite were averaged within a circle with a diameter of about 500 km and the spatial resolution of the PIXIE images from these apogee passes is ~1000 km. However, as long as the averaging area is significantly smaller than the spatial resolution of the pinhole camera itself, the resulting spatial resolution of the X-ray profiles is basically determined by the spatial resolution of the camera, i.e., 1000 km. The profiles of the calculated X-ray production from the electron measurements were smoothed by a running average of 140 seconds (i.e., over 1000 km along the satellite orbit) in order to be comparable to the spatial resolution of the measured X-ray profiles (i.e., 1000 km). Here it should be emphasized that the smoothing of electrons can only be applied along the satellites trajectory and that any structures in the vicinity of this trajectory will not be detected by the satellites but will be within the region used to present the X-ray profiles. From the NOAA-12 passes we had some pitch angle information as the Medium Energy Proton and Electron Detector (MEPED) (30keV-~1000keV) have two sensors looking at 10˚ and 80˚ local zenith angles, which correspond to 0˚-25˚ and 65˚-95˚ pitch angle intervals, respectively. Based on these measurements of both trapped and precipitating electrons we were able to identify the region of isotropic electron precipitation. Assuming that the main energy deposition is occurring at ~100 km altitude the loss cone at the satellite altitude of ~850 km is found to be within ~50˚ pitch angle in the northern hemisphere (>50˚ CGM latitude). As the Total Energy Detector (TED) onboard NOAA-12 only looks within the 0˚-25˚ pitch angle interval and we needed both detectors to establish the electron spectrum (from some eV up to ~1000 keV), our calculated X rays only represent the X-ray production from the most field aligned electrons. Any anisotropy giving increasing electron fluxes towards larger pitch angles, but still within the loss cone, would therefore result in an underestimate of the X-ray production. This is exactly what we observed in the regions of anisotropic electron fluxes as can be seen in Figure 5b, 5c and 5d on page 87 and Figure 7b, 7c and 7d on page 88. From the measurements by the SSJ/4 electrostatic analysers onboard the DMSP satellites we only obtain information about the electron spectra <30 keV and at pitch angles <15˚, well within the atmospheric loss cone as the detector always points toward local zenith. Based on our findings from the NOAA-12 passes we therefore interpreted the regions of smaller calculated X-ray fluxes than directly measured X-ray fluxes, to correspond to the region of anisotropic fluxes of electron precipitation.

As discussed in Section 2.3 and Section 5.1 the X-ray measurements often suffer from poor statistics when spectral information shall be extracted. To obtain sufficient count rates we therefore binned the 63 energy channels of the low energy section of PIXIE into 4 energy bands (channel 20:29, 30:39, 40:49 and 50:59) and the high energy section of the detector into two energy bands (channel 10:15, 16:21). Above channel 21 in the high energy section of PIXIE the auroral X rays are contaminated by the fluorescence peak of Xenon and background noise and were therefore not used [Technical Report]. To further improve the statistics we have chosen areas of no less than 6˚ magnetic latitude and 1 hour MLT sector to obtain the area averaged fluxes in the 6 energy bands. In order to derive a double or single exponential electron spectrum from the X-ray spectrum we proceeded as follows. By minimizing the Chi-squares the single or double electron spectrum that may reproduce the observed X-ray spectrum was found. When more than one electron spectrum passed the Chi-square test we chose the derived electron spectrum that gave the smallest electron energy flux, giving a lower limit of electron energy flux deposited in the ionosphere based on X-ray measurements. To quantify the correlation between derived and directly measured electron spectra we calculated the energy flux from 3 to 100 keV when comparing with NOAA-12 measurements and from 3 to 30 keV when comparing with DMSP measurements, due to the different energy ranges of the detectors. To be in better spatial agreement with the derived electron spectra from the X-ray measurements within the specified area we have used 80 s average electron spectra for these integrations. The results are shown in e.g., Figure 10 and Figure 11 on page 90, Paper 5.

The results regarding the directly measured energy flux and the energy flux derived from the X-ray measurements were summarized in Figure 12 on page 92, Paper 5, i.e., from 8 passes (5 from the morning sector and 3 from the midnight sector) during the substorm events of July 31 and September 4. Compared to the energy flux derived from X rays, the energy fluxes from DMSP measurements were found to be systematically underestimated. The energy fluxes measured by NOAA-12 did not show that tendency but were in very good agreement with the energy flux derived from PIXIE. The discrepancies might be explained by the lack of pitch angle information from the DMSP and thus we might have included regions of anisotropic electron fluxes which will give more X rays than can be produced by the electrons measured by DMSP. A similar comparison of PIXIE data and DMSP electron measurements presented by Anderson et al. [1998] which generally were found to correlate very well, does also show some regions of discrepancies by a factor of ~3, which may be explained by the presence of anisotropic electron fluxes. We conclude that the derived electron energy spectra from PIXIE seem to give rather good estimates of the energy deposition into the ionosphere. However, when the energy fluxes are derived from electron measurements at small pitch angles, as is the case for the DMSP measurements, they can easily be underestimated. To summarize this part of Paper 5:

1. In order to calculate the X-ray production from electron spectra we found that the sum of two exponentials may represent the electron spectra fairly well both in the midnight and the morning sector. In the very high energy range of the electron measurements a Kappa function would probably have made a better fit, but the uncertainties introduced by using the exponentials are probably very small as the fluxes at these high energies are very low.

2. Through the region of localized maximum we found good spatial and quantitative correlation between observed X rays and the X-ray production estimated from the directly measured electron distribution. In the region of isotropic electron fluxes the correspondence was often close to the statistical errors of the X-ray measurements and the discrepancies observed outside this region were most probably due to anisotropic electron fluxes at pitch angles outside the detectors FOV but still within the atmospheric loss cone.

3. By fitting the X-ray spectra by double or single exponentials we have developed a method of deriving electron spectra and the energy deposition into the ionosphere which corresponds within a factor of 2 to the directly measured energy fluxes. When the pitch angle distribution within the loss cone is not known, energy fluxes derived from in-situ electron measurements can very well be underestimated. Thus the energy flux derived from the X rays probably gives a better estimate of the energy flux deposited in the ionosphere.

5.5. The localized morning maximum in the recovery phase

The global images from PIXIE and the time analysis of X-ray features along the auroral zone were used to determine the location and temporal extension of the localized maximum of X-ray emission in the morning sector. We therefore know that 3 of the DMSP satellite passes in the southern hemisphere during the 2 events all occurred during the early stage or just before the morning maximum appeared (see Plate 2 on page 91, Paper 5).

In Paper 2 we suggested that either (1) a wave-particle interaction or (2) scattering due to interaction with the magnetopause might be the mechanism that causes the morning maximum of X-ray emission. The spectrograms shown in Plate 2 on page 91, Paper 5 enable us to examine these hypothesis in more detail. The spectrograms are obtained from passes through the region of localized X-ray emission prior to and during the very beginning of this morning maximum. In all the three panels we can identify a broad peak in the energy range 2-10 keV at rather low latitudes (~64˚-68˚) which corresponds to the location of the observed X rays. The observation of this broad peak at ~2-10 keV in the DMSP data during these two events excludes some of the proposed mechanism for the morning maximum of X-ray emission.

1. The morning maximum observed during these two event can not be explained by the scattering of electrons at the magnetopause, as the X-ray emission (as well as the broad peak in the electron spectrograms) is observed well below 70˚ CGM latitude and consequently the field lines are probably well within the magnetopause.

2. The broadness of the peak indicates no monoenergetic beam, a signature which is usually related to arcs and inverted V events in the pre-midnight sector caused by parallel electric fields and unlikely to be observed at the dawnside.

3. The broad peak is observed too early to be caused by a mechanism triggered by the drifting electrons from the injected particles in the substorm onset region near midnight. For the September 4 event the broad peak is present both at passes prior to and after the onset of the localized morning maximum but varies in intensity. This does not prevent the arrival of drifting electrons to increase the effect of the mechanism.

However, the broad peak may be consistently interpreted as caused by a wave-particle interaction which is more or less continuously present in the morning region and that the strength of the process depends on the anisotropic fluxes of electrons. The shape of the observed spectra in our study indicates that the wave-particle interaction acts on electrons down to a few keV (see also Figure 10 and Figure 11 on page 90, Paper 5). Then we arrive at a

similar conclusion as Jelly and Brice [1967] did, as they suggested that the anisotropy of unstably quasi-trapped electrons is largely determined by the loss cone and hence the instability is determined solely on the flux level, i.e., if the flux exceeds the threshold for the instability to work. This threshold is known as the maximum stable limit for fluxes of trapped energetic electrons proposed by Kennel and Petscek [1966]. However, Jentsch [1976] has shown that an anisotropy is established without introducing the loss cone and the conclusion may therefore be modified at this point, as will be discussed below. When the electron cloud injected at substorm onset enters this region the wave-particle interaction increases and will go on as long as there are sufficient fluxes of anisotropic trapped electrons. The September 4 event occurred in the recovery phase of a magnetic storm and it is therefore likely that there existed sufficient trapped electron fluxes from previous magnetic activity for the wave-particle interaction to work. The July 31 event took place after a long quiet period and the number of trapped electrons was probably lower. This may explain why the broad peak is more pronounced in the September 4 event than the July 31 event.

For parallel propagating waves the Doppler-shifted electron cyclotron wave-particle interaction involving VLF frequencies will act upon electrons with energies $>E_{c\,\|} = {}^1/_2\, m v_\|^2$, where $v_\|$ is the resonant parallel velocity component. The resonance condition for parallel propagating waves, linear approximation is given by (18) and, when all terms are used, by (19).

$$E_{c||} = \frac{B^2}{8\pi n}\frac{\Omega}{\omega} \tag{18}$$

$$E_{c||} = \frac{B^2}{8\pi n}\frac{\Omega}{\omega}\left(1-\frac{\omega}{\Omega}\right)^3 \tag{19}$$

where B is the magnetic field strength, n is the electron density, ω is the wave frequency and Ω is the electron gyro frequency. ω is usually found to be $\sim{}^1/_2\Omega$, which lower the parallel resonant energy by a factor of 8 compared to the linear approximation often used (18). Modelling of wave growth-rates based on Kennel and Petscek [1966], which can account for the observed features have been performed by Jentsch [1976] using n=10 cm^{-3} and electron energies >40keV. The electron energy was partly chosen to avoid the effect of the convective electric field on the electron drift trajectories and his results do not exclude lower electron energies to be involved in the wave-particle interaction. He performed his calculations of wave growth rates for 3 different magnetic field models and it should be noticed that the most realistic magnetic field model, i.e., a model by Mead [1964] resulted in a maximum anisotropy and a maximum wave growth around 5-9 MLT, while introducing a convective electric field tended to shift the maximum anisotropy towards noon. As he used an isotropic electron distribution to model the injected electrons and no loss mechanism were introduced, the anisotropic electron fluxes solely resulted from the different drift velocities for electrons at different pitch angles in the magnetic and the electric field, i.e., no loss cone was needed to obtain the anisotropic fluxes. In a survey study of ELF/VLF waves at geosynchronous orbit Parrot and Gaye [1994] reported that chorus of 400-700 Hz show a distinct peak between 6-9 MLT.

Simultaneous measurements of VLF waves and the angular distribution of electron fluxes in the morning sector are scarce, but a study by Isenberg et al. [1982] based on measurements from the P78-2 (SCATHA) satellite reports some interesting results for the

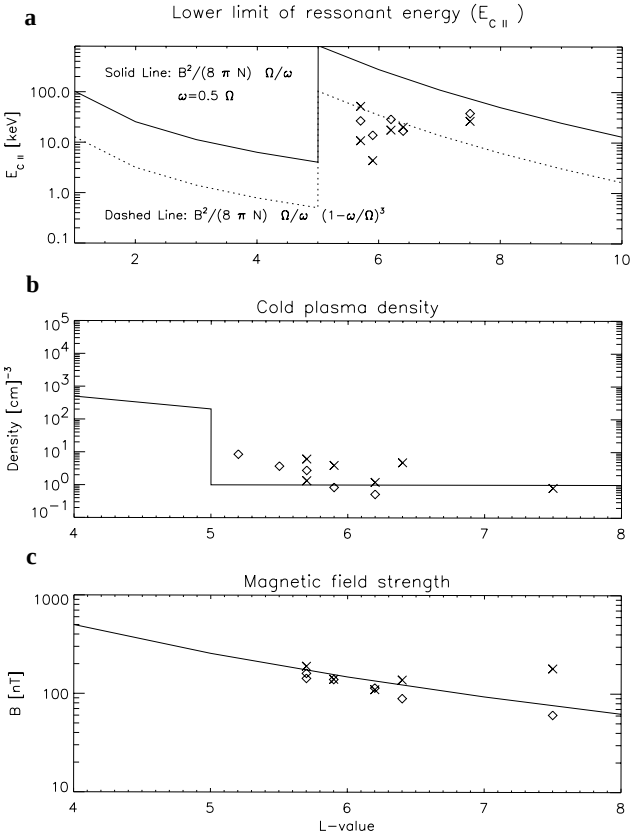

Figure 19. Measurements from Isenberg et al. [1982] plotted as a function of radial distance. In all panels the diamonds indicates the values identified by Isenberg et al. [1982] and the crosses are the values identified by us. (a) The lower energy level of electrons ($E_{c\,\|}$) that interact with VLF waves. Solid line shows the profile calculated by Lyons and Williams [1984]. (b) Densities inferred from (19). Solid line is the density profile used by Lyons and Williams [1984] for the profile in (a). (c) The magnetic measurements onboard the SCATHA satellite. Solid line is the simple dipole field strength.

purpose of this study. The satellite was in a quasi-geosynchronous orbit and equipped with a number of particle and wave experiments. Examining angular electron distribution in the energy range from 12 to 81.5 keV and VLF frequencies from 0.4 to 3.0 kHz they found that the dawnside chorus between 5.3 <L<7.8 is generated by substorm-injected, anisotropic fluxes of electrons with energies between 10 keV and 100 keV. Taking into account the pitch angle distribution of the electrons, the observed waves can very well be interacting with electrons down to ~4-20 keV in the vicinity of the loss cone. It should also be noticed that wave measurements >3kHz were not available and consequently they have no measurements that could have been correlated with the anisotropic electron fluxes at even lower electron energies. In their data, anisotropic fluxes are clearly seen down to 12.1 keV, which is the lowest channel they show. Depending on the pitch angle distribution this may well be consistent with waves acting on electrons down to a few keV in the vicinity of the loss cone. We may conclude that the study by Isenberg et al. [1982] partly support our interpretation of the broad peak in the electron distribution observed by DMSP to be caused by the scattering due to wave-particle interaction. In Figure 19 we have plotted their data to

show how well they confirm the wave-particle interaction concept. Figure 19a shows $E_{c\,\|}$ as a function of radial distance, Figure 19b shows the derived density using (19) and Figure 19c shows the magnetic field strength. In Figures 19a and 19b the corresponding profiles calculated by Lyons and Williams [1984] are shown by solid lines and in Figure 19c the solid line shows the simple dipole field strength. Lyons and Williams [1984] used the simple dipole field strength and the density profile from Figure 19b to calculate the profile in Figure 19a. The diamonds show the data listed in Table 2 from Isenberg et al. [1982] and the crosses show the values we have determined ourselves from their plots showing simultaneously anisotropic fluxes in specific energies of electrons and wave growth at specific frequencies.

From this part of Paper 5 we summarize:

1. The electron energy spectra observed prior to, at the initial stage of, and after the localized morning maximum of X-ray strongly indicates that the wave-particle interaction is the main mechanism for the enhancements observed.

2. VLF-waves are probably excited more or less continuously by quasi-trapped anisotropic fluxes of electrons from tens of keV up to hundreds of keV and the wave growth are further raised by the arrival of the injected anisotropic fluxes injected at midnight drifted into the morning sector. As Jentsch [1976] has shown, the anisotropy of unstably quasi-trapped electrons will result from the different drift velocities of electrons at different pitch angles and is significantly affected by the magnetic field configuration and the presence of any increased electric field. The loss cone will lead to an even stronger anisotropy. The instability and the strength of wave-particle interaction is therefore determined mainly by the flux level. If the fluxes of electrons exceed the maximum stable limit for fluxes of trapped energetic electrons energy are transferred from the electrons to the waves and the wave growth will act back on the electrons and effectively scatter them into the loss cone [Kennel and Petscek, 1966; Jelly and Brice, 1967]. As long as there is sufficient fluxes of trapped anisotropic electrons the process will go on and thus can account for the prolonged maximum observed.

3. Previous simultaneous measurements of anisotropic electron fluxes and VLF waves give some support for the presence of VLF waves which are able to act upon electrons of energies down to just a few keV.

6. Conclusion and further study

In this thesis we have utilized the remote sensing technique of X rays to examine the development of the energetic electron precipitation during substorms. The main conclusions to be drawn are as follows:

1. The development of substorms does not reveal the same characteristics when examining different electron energies.

2. By measuring at several wavelengths it is possible to examine how different electron energies behave differently during substorm events. Different energies may not have the same onset times or the same source location in the magnetosphere.

3. A common feature seen in the energetic precipitation delayed relative to the substorm onset is a prolonged maximum of precipitation in the morning sector at 5-9 MLT. This is not a common feature when measuring at other wavelengths.

4. The morning maximum of energetic precipitation is most probably caused by the unstable fluxes of quasi-trapped electrons drifting into the morning sector, which exceeds the limit of stability when fresh electrons are injected during the early expansion phase of the substorm. Wave-particle interaction is the mechanism that may explain the precipitation.

5. In contrast to the electron energy derivation based on measurements at other wavelengths X-ray measurements provide the possibility to derive multi-parameter energy characteristics about the electron precipitation. While other remote sensing techniques are contaminated by sunlight or sunlight generated emissions (dayglow) the X rays can be detected both at daytime and nighttime. Thus X rays are found to be favourable in estimating the global energy input into the ionosphere. Compared to the uncertainties regarding energy input estimated from in-situ electron measurements when the angular distribution is not known the derivation of the energy input from X rays will reflect the energy input at all pitch angles.

6. The main problem with the remote sensing technique of X rays is the poor counting statistics which forces either the temporal or the spatial resolution to suffer. However, by integrating properly defined areas the time resolution can be as good as 30 s, which is comparable with the measurements at other wavelengths.

The analysis of the PIXIE data set has so far resulted in some published paper but the data set covering more than three years of continuously measurements has a large potential to reveal information about the dynamics during storms and substorm. Some obvious issues to address are:

1. To calculate the global energy input based on the X-ray measurements of the entire auroral oval.

2. Comparison studies with energy input derived from other wavelengths can be used to evaluate the available inversion techniques on a global scale.

3. Comparison study with cosmic radio absorption, which has the electron density profiles (derived from electron spectra) as input.

4. The total amount of energy deposited into the ionosphere can be correlated with the energy transferred into the magnetosphere (the ε parameter) to examine the portion of the total energy that enters the ionosphere.

The results presented in this thesis have hopefully emphasized that the remote sensing of X rays is a very strong tool to obtain information about the energy transfer through precipitating electrons into the ionosphere. By performing new X-ray experiments utilizing new technology to improve the spatial resolution of X-ray imaging even better estimates of energy transfer into the ionosphere could be made.

References

Akasofu, S.-I., The development of the auroral substorm, *Planet. Space Sci.*, *12*, 273–282, 1964.

Akasofu, S.-I., *Polar and Magnetospheric Substorms*, D. Reidel, Norwell, Mass., 1968.

Akasofu, S.-I., Energy coupling between the solar wind and the magnetosphere, *Space Sci. Rev.*, *28*, 121–190, 1981.

Akasofu, S.-I., D. S. Kimball, and C. I. Meng, The dynamics of the aurora – V. Poleward motions, *J. Atmos. Terr. Phys.*, *28*, 497, 1966.

Anderson, P. C., D. L. Chenette, D. L. McKenzie, J. M. Quinn, M. Grande, and M. Carter, Energetic auroral electron distribution derived from global x-ray measurements and comparison with in-situ particle measurements, *Geophys. Res. Lett.*, *25*, 4105–4108, 1998.

Anger, C. D. et al., An ultraviolet auroral imager for the Viking spacecraft, *Geophys. Res. Lett.*, *14*, 387–390, 1987.

Anger, C. D., T. Fancott, J. McNally, and H. S. Kerr, ISIS-II scanning auroral photometer, *Appl. Opt*, *12*, 1753–1766, 1973.

Barcus, J. R., Balloon observations on the relationship of energetic electrons to visual aurora and auroral absorption, *J. Geophys. Res.*, *70*, 2135–2147, 1965.

Barcus, J. R., and T. J. Rosenberg, Energy spectrum for auroral-zone X rays, 1, Diurnal and type effects, *J. Geophys. Res.*, *71*, 803–823, 1966.

Berger, M. J., and S. M. Seltzer, Bremsstrahlung in the atmosphere, *J. Atmos. Terr. Phys.*, *34*, 85–108, 1972.

Berger, M. J., S. M. Seltzer, and K. Maeda, Energy deposition by auroral electrons in the atmosphere, *J. Atmos. Terr. Phys.*, *32*, 1015, 1970.

Berkey, F. T., V. M. Driatskij, K. Henriksen, B. Hultqvist, D. Jelly, T. I. Shchuka, A. Theander, and J. Yliniemi, A synoptic investigation of particle precipitation dynamics for 60 substorms in IQSY(1964-65) and IASY(1969), *Planet. Space Sci.*, *22*, 255–307, 1974.

Birn, J., M. F. Thomson, J. E. Borovsky, G. D. Reeves, D. J. McComas, R. D. Belian, and M. Hesse, Substorm electron injections: Geosynchronous observations and test particle simulations, *J. Geophys. Res.*, *103*, 9235–9248, 1998.

Bjordal, J., H. Trefall, S. Ullaland, A. Bewersdorff, J. Kangas, P. Tanskanen, G. Kremser, K. H. Saeger, and H. Specht, On the morphology of auroral-zone X-ray events, I, Dynamics of midnight events, *J. Atmos. Terr. Phys.*, *33*, 605–626, 1971.

Brice, N. M., and D. Lucas, Influence of magnetic convection and polar wind on loss of electrons from the outer radiation belt, *J. Geophys. Res.*, *76*, 900–908, 1971.

Calvert, W., H. D. Voss, and T. C. Sanders, A satellite imager for atmospheric X rays, *IEEE Trans. Nucl. Sci.*, *NS-32*, 112–118, 1985.

Chenette, D. C., D. W. Datlowe, W. L. Imhof, T. L. Schumaker, and J. D. Tobin, Global spectroscopy and imaging of atmospheric X-ray bremsstrahlung: Instrumentation and initial results from the PEM/AXIS instrument aboard the Upper Atmosphere Research Satellite, *Proc. SPIE Int. Soc. Opt. Eng.*, *1745*, 16–25, 1992.

Christon, S. P., D. J. Williams, D. G. Mitchell, C. Y. Huang, and L. A. Frank, Spectral characteristics of plasma sheet ion and electron precipitation during disturbed geomagnetic conditions, *J. Geophys. Res.*, *96*, 1–22, 1991.

Codrescu, M. V., T. J. Fuller-Rowell, R. Roble, and D. S. Evans, Medium energy particle precipitation influence on the mesosphere and lower thermosphere, *J. Geophys. Res.*, *102*, 19,977–19,987, 1997.

Cummer, S. A., R. R. Vondrak, N. Østgaard, J. Stadsens, J. Bjordal, D. L. Chenette, M. Brittnacher, and G. K. Parks, Global multispectral auroral iamging of an isolated substorm, *Geophys. Res. Lett.*, -, submitted June,99, 1999.

Datlowe, D. W., W. L. Imhof, and H. D. Voss, X-ray spectral images of energetic electrons precipitating in the auroral zone, *J. Geophys. Res.*, *93*, 8662–8680, 1988.

Eather, R. H., and S. B. Mende, Airborne observations of auroral precipitation patterns, *J. Geophys. Res.*, *76*, 1746, 1971.

Elphinstone, R. D., J. S. Murphree, L. L. Cogger, D. Hearn, M. G. Henderson, and R. Lundin, Observations of changes to the auroral distribution prior to substorm onset, in *Magnetospheric Substorms*, *Geophys. Monogr. Ser.*, vol. 64, edited by J. R. Kan et al., pp. 257–275, AGU, Washington, D. C., 1991.

Elwert, G., *Ann. Physik*, 178, 1939.

Elwert, G., and E. Haug, *Phys. Rev.*, 90, 1969.

Erickson, K. N., R. L. Swanson, R. J. Walker, and J. R. Winckler, A study of magnetospheric dynamics during auroral electrojet events by observation of energetic electron intensity changes at geosynchronous orbit, *J. Geophys. Res.*, *84*, 931–942, 1979.

Fairfield, D. H., The average magnetic field configuration of the outer magnetosphere, *J. Geophys. Res.*, *73*, 7329–7338, 1968.

Frank, L. A., J. D. Craven, K. L. Ackerson, M. R. English, R. H. Eather, and R. L. Carovillano, Global auroral imaging instrument fro the Dynamic Explorer mission, *Space. Sci. Instr.*, *5*, 369, 1981.

Frank, L. A., J. B. sIgwarth, J. D. Craven, J. P. Cravens, J. S. Dolan, M. R. Dvorsky, P. K. Hardebeck, J. D. Harvey, and D. W. Muller, The visible imaging system (VIS) for the Polar spacecraft, *Space Sci. Rev.*, *71*, 297–328, 1995.

Friedel, R., A. Korth, and G. Kremser, Substorm onsets observed by CRRES: Determination of energetic electron source regions, *J. Geophys. Res.*, *101*, 13,137–13,154, 1996.

Germany, G. A., G. K. Parks, M. B. J. Cumnock, D. Lummerzheim, J. F. Spann, L. Chen, P. G. Richards, and F. J. Rich, Remote determination of auroral energy characteristics during substorm activity, *Geophys. Res. Lett.*, *24*, 995–998, 1997.

Germany, G. A., M. R. Torr, P. G. Richards, and D. G. Torr, The dependence of model OI 1356 and N_2 Lyman Birge Hopfield auroral emissions on the neutral atmosphere, *J. Geophys. Res.*, *95*, 7725–7733, 1990.

Gilvin, P., E. Mathieson, and G. C. Smith, Subdivision of a graded density cathode, *Nuclear Instruments and Methods*, *185*, 595–597, 1981.

Goldberg, R. A., J. R. Barcus, L. A. Treinish, and R. R. Vondrak, Mapping of auroral X rays from rocket overflights, *J. Geophys. Res.*, *87*, 2509–2524, 1982.

Gorney, D. J., Satellite-based remote sensing of aurora, in *Quantitative Modelling of Magnetosphere - Ionosphere Coupling Processes*, edited by Y. Kamide and R. Wolf, Kyoto Sangyo University, Kyoto, Japan, 1987.

Håland, S. et al., Magnetospheric and ionospheric response to a substorm: Geotail HEP-LD and Polar PIXIE observations, *J. Geophys. Res.*, 1999. accepted for publ. May 1999.

Hardy, D. A., M. S. Gussenhoven, and E. Holeman, A statistical model of auroral electron precipitation, *J. Geophys. Res.*, *90*, 4229–4248, 1985.

Hartz, T. H., and N. M. Brice, The general pattern of auroral particle precipitation, *Planet. Space Sci.*, *15*, 301–329, 1967.

Hones, E. W., The magnetotail: Its generation and dissipation, in *Physics of Solar Planetary Environments*, edited by D. J. Williams, pp. 559–591, AGU, Washington D.C., 1976.

Hones, E. W., Substorm processes in the magnetotail: Comments on "on hot tenous plasmas, fireballs, and boundary layers in the Earth's magnetotail" by L. A. Frank, K. L. Ackerson and R. P. Lepping, *J. Geophys. Res.*, *82*, 5633–5640, 1977.

Hones, E. W., Transient phenomena in the magnetotail and their relation to substorms, *Space Sci. Rev.*, *23*, 393–410, 1979.

Imhof, W. L., J. R. Kilner, G. H. Nakano, and J. B. Reagan, Satellite X-ray mappings of sporadic auroral zone electron precipitation events in the local dusk sector, *J. Geophys. Res.*, *85*, 3347–3359, 1980.

Imhof, W. L., G. H. Nakano, R. G. Johnson, and J. B. Reagan, Satellite obsrevations of bremsstrahlung from widespread energetic electron precipitation events, *J. Geophys. Res.*, *79*, 565, 1974.

Imhof, W. L. et al., The Polar Ionospheric X-ray Imaging Experiment (PIXIE), *Space Sci. Rev.*, *71*, 385–408, 1995.

Isenberg, P. A., H. C. Koons, and J. F. Fennell, Simultaneous observations of energetic electrons and dawnside chorus in geosynchronous orbit, *J. Geophys. Res.*, *87*, 1495–1503, 1982.

Jelly, D., and N. Brice, Changes in Van Allen radiation associated with polar substorms, *J. Geophys. Res.*, *72*, 5919–5931, 1967.

Jentsch, V., Electron precipitation in the morning sector of the auroral zone, *J. Geophys. Res.*, *81*, 135–146, 1976.

Kamiyama, H., Flux of bremsstrahlung photons caused by energetic electrons precipitating into the upper atmosphere, *Rep. Ionosp. Space Res. Jpn*, *20*, 374–394, 1966.

Kan, J. R., L. Zhu, A. T. Y. Lui, and S.-I. Akasofu, A magnetosphere-ionosphere coupling theory of substorms including magnetotail dynamics, in *Auroral Physics*, edited by C.-L. Meng, M. J. Rycroft, and L. A. Frank, pp. 311–321, Cambridge Univ. Press, New York, 1991.

Kaneda, E., M. Takgi, and N. Niwa, Vacuum ultraviolet television camera, *in Proc. 12th Int. Symp. Space Tech. Sci.*. 233–238, 1977.

Kangas, J., L. Lukkari, P. Tanskanen, H. Trefall, J. Stadsnes, G. Kremser, and W. Riedler, On the morphology of auroral-zone X-ray events, IV, Substorm-related electron precipitation in the local morning sector, *J. Atmos. Terr. Phys.*, *37*, 1289–1303, 1975.

Kennel, C. F., and H. E. Petscek, Limit on stably trapped particle fluxes, *J.Geophys. Res.*, *71*, 1–28, 1966.

Khosa, P. N., R. R. Rausaria, and K. L. Moza, Spectrum, angular distribution and polarization of auroral hard X rays, *Planet. Space Sci.*, *32*, 31–39, 1984.

Kokubun, S., and R. L. McPherron, Substorm signatures at synchronous altitudes, *J. Geophys. Res.*, *86*, 11,265–11,277, 1981.

Kulenkampff, H., *Ann. Physik*, *69*, 548, 1922.

Leighton, R. B., *Principles of Modern Physics*, McGraw-Hill,New York, 1959.

Lew, J. A., Drift rate in a dipole field, *J. Geophys. Res.*, *66*, 2681–2685, 1961.

Lorence, L. J., CEPXS/ONELD Version 2.0: A discrete ordinates code package for general one-dimensional coupled electron-photon transport, *IEEE Trans. Nucl. Sci*, *39*, 1031–1034, 1992.

Luhmann, J. G., and J. B. Blake, Calculations of soft auroral bremsstrahlung and Ka line emission at satellite altitude, *J. Atmos. Terr. Phys.*, *39*, 913, 1977.

Lyons, L. R., and D. J. Williams, *Quantitative aspects of magnetospheric physics*, D. Reidel Publishing Company, Dordrecht, Holland, 1st edition, 1984.

Mæhlum, B., and J. Stadsnes, Scattering and absorption of fast electrons in the upper atmosphere, *Physica Norvegia*, *2*, 1967.

McDiarmid, I. B., J. R. Burrows, and E. E. Budzinski, Average characteristics of magnetospheric electrons (140 eV to 200 keV) at 1400 kilometers, *J. Geophys. Res.*, *80*, 73–79, 1975.

McPherron, R. L., C. T. Russell, and M. P. Aubrey, Satellite studies of magnetospheric substorms on August 15, 1968, 9. Phenomenological model for substorms, *J. Geophys. Res.*, *78*, 3131–3149, 1973.

Mead, G. D., Deformation of the geomagnetic field by the solar wind, *J. Geophys. Res.*, *69*, 1181–1195, 1964.

Meng, C. I., and R. E. Huffman, Ultraviolet imaging from space of the aurora under full sunlight, *Geophys. Res. Lett.*, *11*, 315, 1984.

Meng, C. I., R. E. Huffman, F. D. Greco, and R. Eastes, *EOS*, *68(16)*, 396, 1987.

Meng, C. I., A. L. Snyder, and H. W. Kroehl, Observations of auroral westward travelling surges and electron precipitation, *J. Geophys. Res.*, *83*, 575–585, 1978.

Mizera, P. F., D. J. Gorney, and J. Roeder, Auroral X-ray images from DMSP-F6, *Geophys. Res. Lett.*, *11*, 255, 1984.

Mizera, P. F., J. G. Luhmann, W. A. Kolasinski, and J. B. Blake, Correlated observations of auroral arcs, electrons, and X rays from a DMSP satellite, *J. Geophys. Res.*, *83*, 5573–5578, 1978.

Newell, P. T., and C.-I. Meng, Ionospheric projections of magnetospheric regions under low and high solar wind pressure conditions, *J. Geophys. Res.*, *99*, 273–286, 1994.

Oguti, T., E. Kaneda, M. Ejiri, S. Sasaki, A. kadokura, T. Yamamoto, K. Hayashi, R. Fujii, and K. Makitea, Studies of aurora dynamics by aurora-TV on the Akebono (EXOS-D) satellite, *J. Geomagn. Geoelectr.*, *42*, 555, 1990.

Omholt, A., *The optical aurora*, Springer, New York, 1971.

Østgaard, N., J. Bjordal, J. Stadsnes, and E. Thorsen, 1999a, PIXIE data processing at the University of Bergen. *Rep. 1999-05, ISSN 0803-2696*, University of Bergen.

Østgaard, N., J. Stadsnes, K. Aarsnes, F. Søraas, K. Måseide, M. Smith, and J. Sharber, Simultaneous measurements of X rays and electrons during a pulsating aurora, *Ann. Geophys.*, *16*, 148–160, 1998.

Østgaard, N., J. Stadsnes, J. Bjordal, R. R. Vondrak, S. A. Cummer, D. Chenette, G. K. Parks, M. J. Brittnacher, and D. L. McKenzie, Global scale electron precipitation features seen in UV and X rays during substorms, *J. Geophys. Res.*, *104*, 10,191–10,204, 1999c.

Østgaard, N., J. Stadsnes, J. Bjordal, R. R. Vondrak, S. A. Cummer, D. Chenette, M. Schulz, and J. Pronko, Localized maximum of X-ray emission in the morning sector caused by drifting electrons, *J. Geophys. Res.*, –, –, 1999b. submitted Sept 1999.

Østgaard, N., J. Stadsnes, J. Bjordal, R. R. Vondrak, S. A. Cummer, D. C. M. Schulz, G. K. Parks, M. J. Brittnacher, D. L. McKenzie, and J. G. Pronko, Global X-ray emission during an isolated substorm - A case study, *J. Atmos. Terr. Phys. - Special Issue*, –, –, 1999d. submitted Aug 1999.

Parks, G. K., F. V. Coroniti, R. L. McPherron, and K. A. Anderson, Studies of the magnetospheric substorms, 1, Characteristics of modulated energetic electron precipitation occurring during auroral substorms, *J. Geophys. Res.*, *73*, 1685–1696, 1968.

Parrot, M., and C. A. Gaye, A statistical survey of ELF waves in a geostationary orbit, *Geophys. Res. Lett.*, *21*, 2463–2466, 1994.

Perrault, P., and S. I. Akasofu, A study of magnetic storms, *Geophys. J. R. Astrom. Soc.*, *54*, 547, 1978.

Petrinec, S. M., J. Mobilia, D. Chenette, W. L. Imhof, and F. Fenrich, Statistical survey of auroral X-ray emissions: PIXIE observations, in *Proceedings of the International Conference on Substorms*, vol. 4, edited by Y. Kamide, pp. 809–812, Terra Sci., Tokyo, 1998.

Pulkkinen, T. I., A study of magnetic field and current configurations in the magnetotail at the time of a substorm onset, *Planet. Space Sci.*, *39*, 833–845, 1991.

Pytte, T., and H. Trefall, Auroral-zone electron precipitation events observed before and at the onset of negative magnetic bays, *J. Atmos. Terr. Phys.*, *34*, 315–337, 1972.

Rees, M. H., Auroral ionization and excitation by incident energetic electrons, *Planet. Space Sci.*, *11*, 1209–1218, 1963.

Rees, M. H., Ionization in the Earth's atmosphere by aurorally associated bremsstrahlung X rays, *Planet. Space Sci.*, *12*, 1093–1108, 1964.

Rees, M. H., and D. Luckey, Auroral electron energy derived from ratio of spectroscopic emissions, 1. Model computations, *J. Geophys. Res.*, *79*, 5182, 1974.

Reeves, G. D., R. D. Belian, and T. A. Fritz, Numerical tracing of enegetic particle drifts in a model magnetosphere, *J. Geophys. Res.*, *96*, 13,997, 1991.

Reeves, G. D., T. A. Fritz, T. E. Cayton, and R. D. Belian, Multi-satellite measurements of substorm injection region, *Geophys. Res. Lett.*, *17*, 2015, 1990.

Riedler, W., and H. Borg, High-latitude precipitation of low-energy particles as observed by ESRO 1A, in *Proceedings of Open Meeting of Working Groups of the Fouteenth Plenary Meeting of COSPAR*, edited by S. A. Bowhill, L. D. Jaffe, and M. J. Rycroft. *Akademie-Verlag, Berlin*, 1397–1403, 1972.

Robinson, R. M., G. T. Davidson, R. R. Vondrak, W. E. Francis, and M. Walt, A technique for interpretation of auroral bremsstrahlung X-ray spectra, *Planet. Space Sci.*, *37*, 1053–1062, 1989.

Robinson, R. M., and R. R. Vondrak, Validation of techniques for space based remote sensing of auroral precipitation and its ionospheric effect, *Space Sci. Rev.*, *69*, 331–407, 1994.

Roederer, J. G., *Dynamics of Geomagnetically Trapped Radiation*, Springer Verlag, New York, 1970.

Rogers, E. H., D. F. Nelson, and R. C. Savage, Auroral photography from a satellite, *Science*, *183*, 951, 1974.

Rostoker, G., and T. Eastman, A boundary layer model for magnetospheric substorms, *J. Geophys. Res.*, *92*, 12,187–12,201, 1987.

Sauter, F., *Ann. Physik*, 404, 1934.

Seltzer, S. M., and M. J. Berger, Bremsstrahlung in the atmosphere at satellite altitudes, *J. Atmos. Terr. Phys.*, *36*, 1283–1287, 1974.

Sergeev, V. A., N. P. Dmitrieva, and E. S. Bakova, Triggering of substorm expansion by the IMF directional discontinuities: Time delay analysis, *Planet. Space Sci.*, *34*, 1109–1118, 1986.

Sergeev, V. A., E. M. Sazhina, N. A. Tsyganenko, J. Å. Lundblad, and F. Søraas, Pitch angle scattering of energetic protons in the magnetotail current sheet as the dominant source of their isotropic precipitation into the nightside ionosphere, *Planet. Space Sci.*, *31*, 1147–1155, 1983.

Sergeev, V. A., L. I. Vagina, R. Elphinstone, J. S. Murphree, D. J. Hearn, L. L. Cogger, and M. L. Johnson, Comparison of UV optical signatures with the substorm current wedge as predicted by an inversion algorithm, *J. Geophys. Res.*, *101*, 2615–2627, 1996.

Sharber, J. R., R. A. Frahm, R. Link, G. Crowly, J. D. Winningham, E. E. Gaines, R. W. Nightingale, D. L. Chenette, B. J. Anderson, and C. A. Gurgiolo, UARS Particle Enviroment Monitor observations during the november 1993 storm: Auroral morphology, spectral characterization, and energy deposition, *J. Geophys. Res.*, *103*, 26,307–26,322, 1998.

Shiokawa, K. et al., High-speed ion flow, substorm current wedge, and multiple Pi 2 pulsations, *J. Geophys. Res.*, *103*, 4491–4507, 1998.

Sibeck, D. G., R. E. Lopez, and E. C. Roelof, Solar wind control of the magnetopause shape, location, and motion, *J. Geophys. Res.*, *96*, 5489–5495, 1991.

Sletten, A., J. Stadsnes, and H. Trefall, Auroral-zone X-ray events and their relation to polar magnetic substorms, *J. Atmos. Terr. Phys.*, *33*, 589–604, 1971.

Stadsnes, J., K. Aarsnes, and J. Bjordal, X-ray imaging of the aurora, *Adv. Space. Res*, *20*, 1043–1054, 1997.

Stadsnes, J., K. Aarsnes, J. Bjordal, F. Søraas, and K. Måseide, Pulsaur II: Observations of aurora and bremsstrahlung X rays in a pulsating aurora, *Proceedings 12th ESA Symposium on European Rocket and Balloon Programmes and Related Research, Lillehammer, Norway*, 239–243, 1995.

Stadsnes, J., J. Bjordal, E. Thorsen, N. Østgaard, D. L. Chenette, G. K. Parks, and M. Brittnacher, Temporal characteristics of energetic electron precipitation during substorm onset and expansion phase, *EOS*, *79*, 1998. AGU fall meeting, SM41B-05.

Steele, D. P., and D. J. McEwen, Electron auroral excitation efficiencies and intensity bratios, *J. Geophys. Res.*, *95*, 10,321, 1990.

Storm, E., and H. I. Israel, 1967, Photon cross section from 0.001 to 100 MeV for elements 1 through 100. *Rep. LA - 3753*, Los Alomos Scientific Laboratory.

Strickland, D. J., and D. E. J. Anderson, Dependence of auroral FUV emissions on the incident electron spectrum and neutral atmosphere, *J. Geophys. Res.*, *88*, 8051, 1983.

Torr, M. R. et al., A far ultraviolet imager for the international solar-terrestrial physics mission., *Space Sci. Rev.*, *71*, 329–383, 1995.

Tseng, H. K., R. H. Pratt, and C. M. Lee, Electron bremsstrahlung angular distribution in the 1-500 keV enery range, *Phys. Rev.*, *19*, 187–195, 1979.

Tsyganenko, N. A., Modelling the Earth's magnetospheric magnetic field confined within a realistic magnetopause, *J. Geophys. Res.*, *100*, 5599–5612, 1995.

Tsyganenko, N. A., and A. V. Usmanov, Determination of the magnetospheric current system parameters and development of experimental

geomagnetic field models based on data from IMP and HEOS satellites, *Planet. Space Sci.*, *30*, 985, 1982.

Vij, K. K., D. Vekatesan, W. R. Sheldon, J. W. Kern, J. R. Benbrook, and B. A. Whalen, Simultaneous investigation of parent electrons and bremsstrahlung X rays by rocket-borne detectors, *J. Geophys. Res.*, *80*, 2869–2875, 1975.

Walker, R. J., and C. T. Russell, Solar-wind interactions with magnetized planets, in *Introduction to Space Physics*, edited by M. G. Kivelson and C. T. Russell, pp. 164–182, Cambridge Univ. Press, England, 1995.

Walt, M., L. L. Newkirk, and W. E. Francis, Bremsstrahlung produced by precipitating electrons, *J. Geophys. Res.*, *84*, 967, 1979.